

# Active Microwave Radar Observations of Weddell Sea Ice

Mark R. Drinkwater

Jet Propulsion Laboratory, MS 300-323  
California Institute of Technology  
4800 Oak Grove Drive  
Pasadena, CA 911 09  
USA

Submitted to: American Geophysical Union  
*Antarctic Research Series*

Date Prepared: September 16, 1996

Date Accepted: ????

---

## TABLE OF CONTENTS

<b>1. INTRODUCTION</b>	<b>1</b>
<b>2. ANTARCTIC MICROWAVE RADAR IMAGING</b>	<b>2</b>
2.1. ERS SAR	2
2.2. ERS SCATTEROMETER	3
2.3. ISSUES OF RADAR TIME-SPACE SAMPLING DIVERSITY	3
<b>3. RADAR CHARACTERISTICS OF WEDDELL SEA ICE</b>	<b>4</b>
3.1. LARGE SCALE CHARACTERISTICS OF THE WEDDELL SEA	4
3.1.1. Summer Scatterometer Images	5
3.1.2. Winter Scatterometer Images	6
3.1.3. Scatterometer Time-Series	7
3.2. MICROWAVE BACKSCATTER SIGNATURES OF WEDDELL SEA ICE	8
3.2.1. Calibration and Backscatter Calibration Accuracy	9
3.2.2. Regional C-band Backscatter Variability	9
3.2.3. Component Ice Signatures	12
3.2.3.1. The Ice Margin and Pancake Ice Floes	13
3.2.3.2. Nilas	14
3.2.3.3. White Ice Floes	15
3.2.3.4. Smooth First-Year Ice Floes	15
3.2.3.5. Rough First-Year Ice Floes	16
3.2.3.6. Multiyear Ice Floes	16
3.2.4. Snapshot Signature Summary	17
3.3. SEASONAL BACKSCATTER VARIABILITY	18
3.3.1. Summer and Winter SAR Image Characteristics	19
3.3.2. The Summer - Autumn Transition	20
3.3.3. Meltponding	21
<b>4. WEDDELL SEA ICE DYNAMICS</b>	<b>21</b>
4.1. TRACKING ICE SPATIAL MOTION ON WEDDELL	21
4.1.1. GPS Validation of Ice Velocity	22
4.1.2. Ice Kinematics Timeseries	22
4.2. RHEOLOGICAL RESPONSE	24
4.3. SYNOPTIC SCALE MOTION TRACKING	25
<b>5. CONCLUSIONS</b>	<b>25</b>
<b>6. ACKNOWLEDGMENTS</b>	<b>27</b>
<b>7. REFERENCES</b>	<b>28</b>
<b>8. FIGURES</b>	<b>32</b>
<b>9. TABLES</b>	<b>34</b>

## 1. Introduction

During this century, a number of scientific expeditions have been carried out to study the general sea-ice characteristics and circulation patterns in the Weddell Sea [Brennecke, 1921; Schnack-Schiel, 1987; Augstein *et al.*, 1991; Lemke, 1994]. Direct observations have, however, been limited to the eastern and central regions due to a nearly continuous, impenetrable perennial ice cover in the southwestern and western Weddell Sea. Indeed, the early "Endurance" and "Deutschland" drift expeditions were restricted to the central part of the Weddell Sea; and the recent 1992 US-Russian drift-station experiment, though situated on a perennial ice floe in the southwestern Weddell Sea [Drinkwater and Lytle, 1996], was positioned off the shelf-break over the deep ocean basin [ISW Group, 1993].

Results to date indicate ocean circulation is dominated by the Weddell Gyre, with a southward current along the east coast and a northward flowing westerly boundary current along the shelf edge at about 55°W off the Antarctic peninsula [Orsi *et al.*, 1993; Fahrbach *et al.*, 1994; Muench and Gordon, 1995]. Anticyclonic circulation is driven by easterly winds in the north and northerly winds in the southern part of the Weddell Sea. Passive microwave images (courtesy NSIDC) together with the results of large scale sea ice models [Fischer, 1995] generally indicate perennial sea ice with increased thicknesses and concentration in the south west as a result of the large scale atmospheric forcing and simulated ice drift. But to-date few direct spatial or temporal observation datasets are available with which to validate such general patterns,

Recently, observations with active microwave radar remote sensing techniques have enabled mapping of various sea-ice regimes within the Weddell Sea together with their dynamics. The spatial resolution advantage which microwave radar has over passive microwave radiometers is the factor of  $1 \times 10^3$  improvement, from 25 km to 25 m. Synthetic aperture radar (SAR) images available from various satellite instruments now provide information on the small-scale character of the ice cover, and on a scale which enables direct measurement of the areal fraction of open water to be quantified, together with the proportion and location of perennial ice. The main limitations of SAR are their size (100 x 100 km square) and temporal and spatial sampling issues, but a new technique of producing enhanced resolution (12 km) full-polar images now also enable large-scale dynamics of the Southern Ocean sea-ice cover to be analysed and quantified.

This paper first introduces the C-band (5.3 GHz) sensor systems used in this study, together with some of the important and relevant sampling issues and limitations of satellite microwave radar. Second, a broad description of the backscatter characteristics of Weddell Sea ice, together with its regional and seasonal variations is provided. Third, a high resolution description of the microwave signatures of the primary components of the ice cover is given, together with supporting information obtained from shipborne scatterometer and surface measurements. Finally, the regional and basin-wide ice dynamics are described using a combination of mesoscale SAR, buoy and Scatterometer ice kinematics products.

## 2. Antarctic Microwave Radar Imaging

Since 1991, the European Space Agency (ESA) two satellites; ERS-1 (July 1991 - June 1996) and ERS-2 (April 1995- present) have acquired microwave radar data of the Weddell Sea. The Active Microwave instrument (AMI) on board ERS has two C-band modes; an imaging SAR and Scatterometer (E-Scat), and each allow vv-polarized backscatter ( $\sigma_{vv}^0$ ) data to be collected (i.e. wavelength  $\lambda = 5.6$  cm). When the AMI is not in SAR imaging mode it allows E-Scat (non-imaged) backscatter values to be continuously recorded,

### 2.1. ERS SAR

These two ESA satellites are each equipped with SAR. Presently, SAR is the only instrument directly capable of acquiring all-weather (day or night), frequent repeat, high-resolution (25 m), 100 km-swath digital images of Antarctic sea-ice [Drinkwater, 1995a]. High data-rate SAR image data require direct broadcast and recording in the region of interest [ESA/Earthnet, 1992]. Weddell Sea SAR data are recorded in two locations, the German Antarctic Receiving Station (GARS) situated at Gen. Bernardo O'Higgins station, and the Japanese Syowa station [Drinkwater, 1996]. GARS allows acquisition of SAR images of the Weddell and Bellingshausen Seas during periodic 6 week campaigns while Syowa enables Weddell Sea data east of the Greenwich meridian to be acquired upon request. Weddell Sea image acquisition is therefore limited specifically to periods when the SAR is switched on within a receiving station mask, and which coincide with periods of operation of these stations.

## **2.2. ERS Scatterometer**

To date, the principal focus for measurements in the ERS Scatterometer (EScat) mode of the AMI has been the estimation of ocean surface wind vectors across a 500 km swath. Although data are acquired continuously when the Synthetic Aperture Radar (SAR) imaging mode is off, this information has barely been exploited outside the traditional scope of wind speed and direction measurement. These low bit-rate EScat data, with an intrinsic resolution of ~50 km, do not require direct station transmission and are tape recorded and downlinked to more accessible ESA ground stations. Scatterometer  $\sigma_{vv}^0$  data can therefore be collected at times and in some regions where direct SAR downlink is impossible. Thus, extensive daily coverage of the ERS-1 scatterometer is particularly valuable due to the lack of data reception in the AMI SAR mode when Antarctic receiving stations are closed. This is especially true in the Weddell Sea, because of the “campaign-style” operation of GARS and limited access to Syowa. Similarly, a large portion of the Southern Ocean sea-ice cover can not be imaged by SAR in the Pacific sector owing to the lack of a receiving station in this locality.

Operationally, it is impossible to obtain enough SAR images in a short enough time span with which to effectively map ephemeral sea-ice conditions. Instead, a method is proposed using data acquired in the EScat mode for mapping sea-ice characteristics over the entire Southern Ocean ice cover. Recent advances in sea-ice image generation from Scatterometer data [Long *et al.*, 1993; Drinkwater *et al.* 1993a] enable complementary, medium-scale resolution images to be made from ERS-1 data. This method allows construction of enhanced resolution (~12 km) scatterometer images from the backscatter data record, and, by virtue of the wider swath and larger coverage allows mapping of the entire sea-ice cover in a few days [Drinkwater *et al.*, 1993a]. The product is a weekly average sea ice picture, of comparative use to SSM/I passive microwave sea-ice data products. It is proposed that this product be used to track regional-scale spatial and temporal changes in the sea ice cover around the entire Antarctic coast. For the first time, combined C-band ERS SAR and Scatterometer microwave images therefore enable uninterrupted coverage of this geographic region at both high (25 m) and medium-scale (~12 km) resolution.

## **2.3 . Issues of Radar Time-Space Sampling Diversity**

One of the priorities for scientific studies of polar ice and snow is high spatial and temporal coverage, due to the short timescales of variability. Exploitation of radar data, particularly in studies related to the mapping and monitoring of the sea-ice cover, was one of the main driving forces

behind inclusion of the SAR instrument on board ERS - 1 [see Drinkwater, 1995]. A large number of sea-ice studies are currently being performed using Arctic Ocean SAR data received at a number of northern hemisphere ground stations (such as Fairbanks, Alaska and Kiruna, Sweden). These SAR receiving stations enable the majority of the northern hemisphere sea-ice cover to be mapped using the SAR. However, much less coverage is possible of the more extensive sea-ice cover around Antarctica, and in particular in the Weddell Sea, due to the limited operating times of GARS and Syowa. The result is a high resolution SAR image database, which is at best discontinuous in space and time,

The key advantage of EScat is that it operates whenever the SAR is switched off, continuously retrieving information from the Weddell Sea without the necessity of a local receiving station. The wider EScat swath provides more frequent, and broader incidence angle ( $20^\circ \leq \theta \leq 60^\circ$ ) coverage in a given location. This low-bit-rate (LBR) data source is essential to fill in areas of sparse temporal and spatial SAR coverage of the Antarctic ice cover. Until now, the intrinsic low resolution of the EScat data is the main reason why they have not been used in such applications. Nevertheless, the approach described by Drinkwater *et al.* (1993a) produces weekly backscatter maps of the entire Southern Ocean sea-ice cover at a resolution ( $\sim 12$  km) higher than present conventional alternatives such as the SSM/I passive microwave radiometers. EScat images form an uninterrupted sequence of C-band backscatter ( $\sigma_{EScat}^0$ ) of Antarctic sea ice from the beginning of the ERS-1 mission. Since these backscatter images are based on multiple azimuth and incidence angle observations, these data provide greater capability for discriminating ice types and separating of ice from ocean. Coupled with higher frequency passive microwave and finer resolution SAR, these data enable a better understanding of the time sequence and seasonal history of Antarctic sea-ice formation, drift, deformation and decay. Furthermore, medium-scale, resolution EScat images provide the large-scale context within which the high resolution SAR images may be interpreted.

### **3. Radar Characteristics of Weddell Sea Ice**

#### **3.1 Large Scale Characteristics of the Weddell Sea**

The large-scale variability of the mean weekly ice conditions are successfully monitored using EScat enhanced resolution images [Drinkwater *et al.*, 1993a]. EScat images indicate the mean amplitude of the C-band vv-polarized backscattering coefficient ( $A$ ) normalized to a  $40^\circ$  incidence

angle (i.e.  $\sigma_{\theta, Scat}^0$ ). Figure 1 illustrates  $A$  images during, (a) austral summer (ice minimum) during the first week of February 1992 (Julian Days 32-39) and (b) during austral winter ice edge advance (Julian Days 210-216). Each image is masked in the open ocean using an ice edge derived from the mean daily SSM/I zero ice concentration isoline generated for the 7d period of imaging (data courtesy NSI DC). Normalized C-band backscatter images at this incidence angle largely reflect the surface roughness of the sea ice [Drinkwater, 1989; Drinkwater et al, 1995a; Drinkwater and Lytle, in Press]. Generally, smoother less deformed young ice is more reflective and results in the lowest backscatter values, with the most deformed, and thicker ice resulting in the highest  $\sigma_{\theta, Scat}^0$  values. Each of these geophysical characteristics are related to the age and salinity of the sea ice, its history of deformation or flooding throughout ice growth and recession, and the seasonally -dependent temperature. Another factor is snow depth, which is largely related to the age and drift of the ice since formation [Massom et al., In Press]. The following sections describe the general characteristics of these microwave images, together with the specific backscatter signatures generated by various classes of ice.

### 3.1.1. Summer Scatterometer Images

Austral summer sea-ice characteristics and the distribution of perennial ice in the Weddell Sea in 1992 are characterized by Figure 1a. Minimum ice extent typically occurs in February in the Weddell Sea. The 1991 to 1995 EScat timeseries indicates that peak  $A$  values coincide with austral mid-summer ablation [Drinkwater et al., 1995c], and that the timing of this peak varies interannually within the December to mid-March window.  $A$  values in some locations in Figure 1a exceed -5 dB, owing to predominantly rough surface scattering from deformed ice floes during damp snow-surface conditions. Furthermore, regions with the highest residual concentrations of rough perennial ice appear to match the pattern of orange regions. Regional backscatter conditions in the central part of the perennial ice region uniformly exceed -16 dB, and a tongue of material extends eastwards from the tip of the Antarctic peninsula at -63°S, where northwards drifting ice becomes entrained in the Antarctic Circumpolar Current (ACC). A noticeable polynya-type feature also becomes captured by rapid ice edge recession in the location 74°S 32°W.

Three locations of the largest backscatter values, correspond with (i) a cluster of grounded giant icebergs (fragments of A22 and A23) off Berkner Island (at 77°S 45°W), between the Ronne and Filchner ice shelves [Zibordi and Van Woert, 1993], (ii) a region east of the northern Larsen ice shelf (at 66°S 59°W), and (iii) a large residual patch of rough perennial ice between (i) and (ii) in the

region 73° S 45° W. Three small areas of contrasting] y lower backscatter and lower concentration deformed ice occur along the Riiser-Larsen (75° S 30°W), and the east and west ends of the Ronne Ice shelf front (at 77°S 47°W and 74°S 59°W, respectively).

### 3.1.2. *Winter Scatterometer Images*

As the winter cooling progresses, and as less deformed, higher salinity seasonal ice cover grows rapidly to latitudes north of 60° S, A values decline. Figure 1 b shows the mean ice cover in the last week of July, 1992. Samples of Weddell Sea  $\sigma_{HSat}^0$  values from the winter ice cover indicate a typical variation of C-band back scatter between -6 and -23 dB. The pattern of backscatter values is reflective of the structure and variability and dynamics of the sea-ice cover [Drinkwater et al, 1993a]. As the concentration of perennial ice is reduced by diffusion and northwards drift (including melting at the northern ice margin), lower backscatter material grows on the continental shelf region in the predominantly divergent area along the Ronne ice shelf front. Similar low backscatter ice may be observed in the divergence zone in the center of the Weddell Gyre centered at 65°S 20°W.

The streamline of the northward limb of the Weddell Gyre is traced in Figure 1 b by the western margin of a north-west to south-east extending band of low concentration perennial ice. This feature is expressed as a meandering band of higher backscatter (yellow) material tracing the isobaths of the eastern flank of the continental shelf break. This streamer carries old deformed ice away from the site of the grounded icebergs near to the Filchner ice shelf. Winter images from 1991 to the present day also indicate these large icebergs to have played a significant role in preventing influx of thick deformed ice into the south-western Weddell Sea. As in this 1992 image, this periodically causes reduced concentrations of perennial ice in this region during summer and at the beginning of austral freeze-up. The perennial-ice starved region is consequently a high heat flux and vigorous ice growth location during early autumn freeze-up, as katabatic winds and tidal currents carry the ice northwards away from the Ronne ice shelf front. In this argument, slow northwards ice drift on the continental shelf is responsible for the export of ice. Supporting observations for an ice factory on the continental shelf is provided by overlapping FIRS SAR, and SSM/I images [Viehoff et al., 1994; Drinkwater et al., 1994]. SSM/I data confirm the characteristic appearance of higher concentrations of first-year ice in this region north of the Ronne ice shelf front, together with a typical northward dilation in the extent of this feature throughout winter. A more rapid northwards transport of ice off the continental shelf (i.e. in the primary Gyre circulation) drives a shear feature at 68°S 55°W in which smoother first-year ice separates the



slowly moving perennial ice on the continental shelf from the more rapid motion in the streamer of perennial ice originating to the south (described previously).

A further key feature of the winter ice cover is a bright fringe bordering the marginal ice zone. Such high backscatter values were measured in the Weddell Sea in June with a scatterometer, during the Winter Weddell Gyre Study [Drinkwater and Haas, 1994] and such returns correspond with pancake ice formation during high wave activity at the pack ice edge [Early and Long, In Press]. Marginal ice zone returns are described in more detail later.

### *3.1.3. Scatterometer Time-Series*

Time-series maps of the Southern Ocean are a primary application of the Scatterometer imaging technique. SAR can retrieve only limited spatial and temporal coverage of dynamic phenomena observed in response to ocean and atmosphere forcing. The scale of coverage offered by EScat is sufficient to monitor these processes and to place the 25 m resolution 100 km x 100 km SAR images in the context of synoptic or basin-scale ice conditions. The regional timeseries of unmasked images shown in Figure 2 indicates the  $\sigma$  value of radar backscatter during eight weekly periods, at 21-day intervals in 1992. The main characteristic of these relatively high incidence-angle ( $\theta = 40^\circ$ ) images is that sea ice typically demonstrates smoothly-varying isotropic returns in direct contrast to the highly variable returns of open ocean equatorward of the sea-ice margin (indicated by bold white line drawn from the National Ice Center ice edge). Variability in the backscatter from wind-generated waves is large on timescales of several days, and the advantage that is of the EScat is that it views the same location from a number of incidence and azimuthal angles during the period of image integration. This gives a powerful method for separating highly anisotropic or azimuthally-dependent variable wind waves from relatively isotropic and azimuthally independent scattering from collections of sea-ice floes [Early and Long, in Press].

In Figure 2 weekly  $\sigma$  images are generated at intervals from the first week in February (Julian Days 32 - 38) in (a) through the first weeks of July (Julian Days 188-194) in (h). Heavy operation of the SAR mode of the AMI on board ERS-1 is manifested in EScat images as data drop-outs (black areas), particularly in the region around the O'Higgins Station ( $63^\circ 19'S$   $54^\circ 54'W$ ) during early 1992 (i.e. during early testing of the SAR receiving capability). The 1992 minimum ice extent occurs at the end of February, with a subsequent rapid north-eastwards advance during the onset of austral winter, under predominantly thermodynamic ice growth [Massom, 1992]. As the Weddell Sea becomes ice-bound, wind- and current-driven ice motion carries some of the large units of

relatively high backscatter sea-ice away from their origins along the coastal and ice shelf margins. The bright patch of perennial ice originating in the southern central Weddell sea in summer is stretched and dilated by shear and divergence as winter progresses, during its northwards drift. A rather characteristic dark area of smooth first-year ice, which appears in Figure 2(c), grows and extends northwards along the continental shelf margin in a distinctive shear boundary, separating continental shelf ice from that driven northwards in the westward limb of Weddell Gyre. This shear margin is expressed as a finger of dark material which appears in (g) and extends and protrudes northwards (at 70°S 50°W) from the area of low backscatter material in the south west Weddell Sea basin. This shear margin eventually dissects the distinctive perennial ice area on the shelf (along the eastern flank of the Antarctic peninsula), from that perennial ice originating in the central Gyre region.

Of further note in Figure 2 are two summer polynya regions of relatively low ice concentration, which appear in the early series as low backscatter areas in the southern and south-eastern Weddell Sea in Fig. 2a. The latter (at 74°S 30°W), is near enough the ice margin that it becomes captured in the sea-ice retreat by the end of February, 1992 (Fig. 2b). Nevertheless, as the ice margin advances the relatively darker signature of these previously open water areas reappear and become source regions for low backscatter new-ice formation. Undeformed, low back scatter ice is transported away from these locations as it becomes embedded and advected north-westwards in the motion of the Weddell Gyre circulation. As the ice is carried northwards, new seasonal ice is formed particularly along the Ronne ice shelf. By the beginning of May (Figure 2e), a large expanse of low backscatter (dark) has appeared, confirmed in Drinkwater *et al.* (1993a) and Viehoff *et al.* (1994) using I H-W-J SAR images to be the northward expansion in extent of seasonal, undeformed ice produced off the ice-shelf front.

### **3.2. Microwave Backscatter Signatures of Weddell Sea Ice**

Since the launch of MN-1, C-band radar backscatter characteristics of sea ice have been investigated during a number of Weddell Sea surface experiments [1 Drinkwater *et al.*, 1993b; Hosseinmostafa *et al.*, 1995; Drinkwater *et al.*, 1995a; Lytle *et al.*, 1996]. However, most of these have focused on the smaller-scale influences of sea-ice physical properties upon surface-scatterometer measurements, without placing them in the context of satellite radar measurements. In this section, a synthesis is provided of both large- and small-scale measurements. Examples are

provided together with corresponding field observations and surface validation from the 1992 Winter Weddell Gyre Study (WWGS '92) [Lemke, 1994; Drinkwater and Haas, 1994].

### 3.2.1. *Calibration and Backscatter Calibration Accuracy*

SAR data products received and processed by the German Processing and Archiving Facility (DPAF) must be treated differently than most US processed images, since they are distributed in a full resolution (i.e. 12.5 m pixel spacing), uncalibrated form. According to a study by Bally *et al.* (1995) for these 3-look SAR images (i.e. ESASAR.PRI products), the single 12.5 m pixel 90% radiometric confidence interval is bounded by  $\pm 4.5$  dB. Thus, the probability that the measured intensity lies within a  $\pm 4.5$  dB error bound is 90%, whereas the radiometric accuracy and stability errors are within specifications of a fraction of a dB (Laur *et al.*, 1993).

To calculate the SAR backscattering coefficient ( $\sigma_{SAR}^0$ ) of a distributed target which corresponds to an area of sea ice (N pixels in extent), or a group of pixels in the image, averaging is required. Intensity averaging reduces "speckle" (i.e. radiometric resolution errors). If "block averaging" is used to create a speckle-filtered image, the new equivalent number of looks is modified by the area of block averaging, together with the target area (i.e. number of pixels averaged from target), and is also a function of the incidence angle  $\theta$  (since resolution is range dependent). The resulting confidence interval for an 8 x 8 block-averaged image with 100 m pixel spacing exceeds 90% for  $\pm 1$  dB. With further target averaging, a confidence level exceeding 90% may be achieved for error bounds of  $\pm 0.5$  dB, with a sample box of over 250 pixels (i.e. 16 x 16 pixel box). Over 99% probability of errors less than  $\pm 0.5$  dB may be reached with samples of more than 500 pixels (i.e. 23 x 23 pixel box). Thus, for most of our purposes, having already used a box-filter (8 x 8 window) to reduce the image to 100m pixel spacing, we only have to derive samples from target box areas exceeding 8 x 8 pixels, before the number of looks, necessary to exceed the  $\pm 0.5$  dB error bound at 99% confidence, is satisfied. All samples presented in this paper are from target areas exceeding this minimum threshold area.

### 3.2.2. *Regional C-band Backscatter Variability*

Figure 3 shows a map of the Weddell Sea region, indicating regional locations of several winter SAR image frames listed in Table 1. Associated image probability distribution functions (pdf's) of calibrated backscatter coefficients are shown in Figure 4. Each pdf comprises individual pixel

values from 8 x 8 averaged and calibrated full-resolution SAR PRI images (originally 8000 x 8000 pixels), thereby resulting in 1 x 10<sup>6</sup> pixels per 100 x 100 km frame.

A global pdf histogram in Figure 4 as a black line (shown as bar-histogram with 0.1 dB bin width) shows the combined pdf from all images shown in Figure 3 and listed in Table 1. This sun-mat-y pdf indicates a tri-modal distribution of backscatter  $\sigma_{SAR}^0$ , with distinct components forming peaks at -11.5, -7.0 and -2.5 dB. Individual colored image pdf's indicate that the highest backscatter mode comprises pixels containing glacial ice. Image 5090\_5021, in Figure 3, was acquired in the vicinity of R.V. *Polarstern* as she made a transect along the periphery of the Riiser-Larsen ice shelf. Consequently, this scene contains a significant number of ice-shelf pixels, falling in the range -5 to +5 dB; air temperatures were around -15°C at the time of SAR imaging. The same characteristics are observed in the upper peak in the histogram of image 5387\_5967. This image captures a large iceberg drifting in the outer marginal ice zone (MIZ), north-east of the tip of the Antarctic peninsula (seen in Figure 2g and 2h to the west of the South Orkney islands). Its backscatter values likely exceed those of the ice shelf in the previous example due to its lower latitude and warmer air temperatures. Glacial ice, therefore, comprises a distinct portion of the upper limb of the backscatter distribution in the Weddell Sea, and may conveniently be used in winter to find tabular icebergs of significant size, either in the marginal ice zone or within the interior ice pack. Non-tabular Antarctic icebergs do not always present a uniform target area to the SAR, and rotation and drift with respect to the imaging swath often result in a reduction in contrast between the berg and its sea-ice or ocean background.

The next brightest component distribution is described by the pdf of two contiguous image frames (5387\_5949 and 5387\_5967) along an orbit crossing the marginal ice zone. The peaks in their image histograms overlap almost identically, but for a small transition from the swell-disturbed marginal ice zone to the outer ice edge. Mixtures of brash ice and small first-year ice floes, together with occasional multiyear ice floes characterized the north-western ice swell-rocked margin of the Weddell Sea at the time of SAR imaging [Haas *et al.*, 1992]. Air temperatures and windspeeds at the time of imaging were recorded on board RV *Polarstern* as between -5 and 0°C, and 5 and 10 m/s, respectively. These mixtures have an extremely distinctive signature, with  $\sigma_{SAR}^0$  values ranging between -10 and -5 dB, with a mode at -7.3 dB. Rough surface scattering, occurring from sub-resolution floes, has a distinctively uniform texture, and bears a close resemblance to wave-disturbed northern hemisphere marginal ice zone ice signatures observed by airborne SAR in the Labrador Sea [Livingstone and Drinkwater, 1989; Drinkwater and Squire, 1987]. The further into

the marginal ice zone one traverses, the higher the probability of observing large undeformed first-year ice floes and new ice in leads. These pixels appear as a toe of darker material in the yellow histogram of image 5387\_5949, extending from -12 dB down to around -19 dB.

Similar signatures to the previous marginal ice zone cases, in terms of backscatter amplitude, may be encountered in the central ice pack, but with the obvious distinction of visible ice floes. Image 5249\_4941, shown in Figure 5 (overlapping the path of RV *Polarstern*), contains a typical mixture of perennial and seasonal ice, and was acquired in the outflow path of old ice described by the yellowish streamer in Figure 1b. The mixture histogram combining these two distinctive end-members appears as a broad pdf (in orange) in Figure 4. Shipborne observations, noted by Haas *et al.* (1992) as *Polarstern* traversed the region encompassed by this image (less than 24 hours after SAR imaging - see Table 1), indicated a closed ice cover (100% concentration) comprising level first-year ice punctuated by distinct ridges and rougher multiyear ice in fractions up to 30%. First-year ice was extremely rubble and ridged, particularly around the perimeter of thick multiyear ice floes. The broad pdf, comprises two overlapping distributions without distinctive peaks, due to the continuum of states of the ice ranging from patches of smooth, relatively undeformed first-year ice, to old, deformed snow-covered floes. Individual samples identified in Figure 5 are shown later and used to illustrate the distribution of backscatter in small-scale areas.

The least deformed, or level first-year ice is observed in images 5377\_5031 from the central Weddell Gyre region, and 5449\_5139 from the southern Weddell Sea (Belgrano Bank) region (see Figure 3). The former yields distinctive pdf modes at between -12 and -13 dB. The former is a largely divergent region, in which vast expanses of undeformed white ice alternated with snow-covered stony fields along the transect of *Polarstern* [Haas *et al.*, 1992]. July air temperatures remained stable around -27° C and ice formation was immediate under divergent conditions. The SAR image indicates no open water, and an extremely low ridge density. The example from the southern Weddell (image 5449\_5139) in contrast contains a larger proportion of deformed seasonal ice (with higher ridging density), and a small fraction of grounded icebergs and perennial ice exiting the basin northwards [Viehoff and Li, 1995]. These higher backscatter components of the scene account for the higher pdf mode for image 5449\_5139 in Figure 4, and the tail extending to values exceeding -5 dB. Based on the predominant drift direction, the origin of the old ice and icebergs found in this region appears to be the Filchner ice shelf front, or the location of grounded icebergs A22 and A23. Large 5-10 km diameter high backscatter (-7 to -2 dB) multiyear ice floes are clearly conglomerates of distinct old ice floes cemented together by a matrix of what was likely snow-

covered landfast ice. Floes have broken away and drifted north-westward in the distinctive streamer of bright material shown in Figure 1 b. Similarly, the iceberg chain, described by Viehoff and Li (1995), which originated as one large iceberg from the Filchner ice shelf, subsequently grounded on the broad General Belgrano Bank, on the northern flank of shallow topography over the Berkner Seamount. Ice-motion data obtained from SAR, Scatterometer and buoys provide complementary evidence for this assertion, but further supporting evidence is provided in the form of tracks of deformed sea-ice created as the sea-ice drifts past the location of each of these icebergs (see Viehoff and Li, Figure 9). The ice cover had drifted in an extremely constant fashion northwards, leaving linear tracers of deformed material extending 100 km or more in length in the direction of drift. At a typical drift speed of 16 cm/s north from the iceberg barrier, each feature represents a period of around 1 week. Furthermore, as pointed out by Viehoff and Li (1995), the persistence of such bands (in ice of the icebergs), in time as well as in space ( $\geq 100$  km), can be interpreted as an indication for a relatively homogeneous ice motion field in this location.

In summary, examples from 5377\_5031 and 5449\_5139 indicate that the least deformed first-year ice, observed in large proportions in the Weddell Sea, comprises the leftmost peak in the global pdf (indicated as the black histogram in Figure 4). Old ice and marginal ice on the other hand fill an overlapping range in backscatter to form the central peak in the global pdf. As expected, heavily ridged or deformed first-year ice fall squarely in the middle of this range, and comprise the main peak in image 5090\_5121. The roughness of sea ice in the location of this SAR image are further described by laser altimeter flights made from Polarstern, and mean ridge heights were typically of the order of 1.2 m, with a mean ridge spacing of 54 m [Dierking, 1995]. Therefore, as previously noted in Drinkwater *et al.* (1995a) for the central ice pack, linear mixing of the two end members (i) smooth undeformed ice and (ii) thick perennial ice accounts for a continuum of  $\sigma_{SAR}^0$  values between -19 and -4 dB. Other than the confusion which exists between MY ice and marginal ice zone signatures, the value of backscatter appears closely related to the amount of deformation and ridging density of the ice, or indeed the ice thickness. Although backscatter values may be encountered in the range -20 to -25 dB, for newly growing areas of nilas and grey ice in leads or ice shelf polynya systems, large expanses of such low backscatter material are rarely encountered in the Weddell Sea.

### 3.2.3. *Component Ice Signatures*

Field radar backscatter data were acquired in 1992 using a shipborne C-band microwave

scatterometer, during W WGS '92. The C-band (4.3 GHz) frequency-modulated continuous-wave (FM-CW) radar scatterometer was operated from the port rail of RV *Polarstern* to obtain some of the first shipborne measurements of the C-band microwave scattering properties of Antarctic sea ice in mid-winter [Drinkwater *et al.*, 1995a]. The radar had dual polarization, enabling like- (vv) and cross-pol(hv) data to be acquired at a variety of incidence angles ( $15 \leq \theta \leq 70^\circ$ ). When the ship was stationary, and on-station by an ice floe, (provided the ice was large enough and uniform in extent) the radar was scanned to obtain  $\sigma_{Ship}^o$  measurements as a function of incidence angle and polarization.

The objective of the 1992 winter scatterometer measurements was to provide validation data for ERS-1 SAR observations and to obtain a detailed microwave backscattering catalogue of various ice conditions. In support, detailed surface measurements were made within the footprint of the shipborne radar, after each scan was performed. Surface information comprises snow and ice physical and chemical properties measurements together with structural information [Drinkwater and Haas, 1994]. Overlapping data acquisitions were planned and made possible by the GARS as part of the International Space Year Project [Lemke, 1994].

### 3.2.3.1. The Ice Margin and Pancake Ice Floes

The outer ice margin or MIZ is typically characterized in Antarctica as a high-energy wave environment, where the propagation of waves into the ice edge plays a dominant role in determining the style of ice formation during winter ice advance, and the characteristics of floes during ice-edge recession. The MIZ is typically broad in its extent during ice-edge advance. In 1992, during W WGS '92, a high amplitude swell was experienced along the Greenwich meridian and frazil and pancake young-ice growth was observed for hundreds of kilometers from the ice margin into the seasonal ice zone. Figure 6a shows a photograph taken in June 1992, of these swell-rocked pancakes in the location of Maud Rise. In contrast, after the peak extent in ice extent the ice edge is typically in a recessional mode, and the marginal ice zone usually comprises brash ice and a mixture of small wave broken floes and wave-washed piles of rubble.

In contrast to the situation for nilas and young ice forms found in calm environments, pancakes were found to be almost ubiquitous at the ice margin (along the Greenwich meridian), during ice edge advance in 1992. The occurrence of vast expanses of pancakes and/or streamers with densely packed sub-resolution floes results in an extremely characteristic marginal ice zone signature.

[Drinkwater *et al.*, 1993a; Gohin, 1995; Early and Long, In Press]. Typically riding on the surface of waves, small wave-washed, porous pans often have a high salinity (Figure 6b) and sufficiently high permittivity that there is relatively strong backscatter near nadir. The rate at which  $\sigma_{Ship}^0$  falls with incidence angle, however, appears dependent on the size and packing density of the pancakes, the amount of open water between them, and how wet or deformed their surfaces are. Figure 6b shows the salinity characteristics of a pancake sampled on 13 June, 1992, and Figure 6c contrasts the 13 June radar signature with another site from the following day. The 13 June signature is greater by 10 dB throughout the incidence angle range, with values exceeding -5 dB at 40° incidence or more, due in part to the denser packing of pans, and their rough, deformed and often rafted surfaces. In cases of smaller pancakes spaced by open water, as on 14 June,  $\sigma_{Ship}^0$  falls more rapidly. Gohin (1995) reports an intermediate marginal ice zone signature (in his Figure 15) which appears a composite of signatures originating over combinations of open water and dispersed floes, or low concentration patches of pancakes.

Considerable azimuthal anisotropy is also noted in pancake ice margins in the ERS scatterometer data (Early and Long, in Press), and is likely due to the fact that the pancakes damp out smaller gravity and capillary waves, leaving only long wavelength swell waves. This results in a dominant wave propagation direction sensed by the scatterometer in some circumstances. Future attempts to fit the functional form of the wind relationship may enable the wave propagation direction to be derived.

#### 3.2.3.2. Nilas

Large expanses of recently formed nilas (< 10 cm thick) have rarely been observed during surface shipborne experiments, largely because Weddell Sea experiments have focused on the ice margin, and swell-influenced regions of the seasonal ice pack. Consequently, the total fraction of ice formed under calm conditions is small, and the opportunity to sample large areas other than in recently opened leads or polynyas with scatterometers is rare. Some young ice was observed during W WGS in 1992, which is reported in Drinkwater and Haas (1994). When observed, nilas typically had little or no snow cover other than frost flowers. The typical signature includes large backscatter coefficients at near nadir angles, with a high gradient of  $\sigma_{Ship}^0$ , falling to values less than -20 dB at high incidence angles. As the large sample of calibrated SAR pixel values in Figure 4 testifies, the probability of occurrence of large fractions of new ice and nilas with values below -15



dB is rare in the Weddell Sea, and these areas are generally focused in locations of long-term divergence or in polynyas along the ice shelf margins.

#### 3.2.3.3. White Ice Floes

The mean thin first-year ice or white ice (in the range 30-50 cm thick) signature shown in Figure 7a, is typical of ice observed in the divergent central Weddell Sea region and is an average of 7 individual site measurements made from 1-14 July, 1992 in the location of scene 5377\_5031 (Figure 3). The signature of this relatively smooth, light snow-covered (1-6 cm snowdepth) ice has  $\sigma_{Ship}^o$  values between -24 and -26 dB in the ERS SAR incidence angle range ( $20^\circ \leq \theta \leq 260^\circ$ ), an intermediate gradient of around 0.49 dB/ $^\circ$  (between 20-60 $^\circ$  incidence), and a neutral cross-polarized backscatter curve. Large expanses of white ice were scoured by strong winds, and had snow depths of less than 5 cm. Lytle *et al.* (1996) have shown previously that snow-free young ice (10-30 cm thick) may result in extremely low backscatter values in an equivalent incidence angle range, thereby increasing as the ice ages (in the absence of deformation) and roughens. These results nevertheless infer that smooth, level white ice with a bare ice surface, or shallow snow cover alone do not play a dominant role in driving the backscatter to values shown in the pdf's in Figure 4, and suggest alternatively that ridged portions of sea ice drive up measured SAR values in this extensive region.

#### 3.2.3.4. Smooth First-Year Ice Floes

The mean signature of smooth, level (undeformed) uniform first-year ice floes of Figure 7b is constructed from 9 individual scatterometer samples, each site of which exceeded 60 cm thickness. A distinguishing feature of this signature is that  $\sigma_{Ship}^o$  exceeds that of the white ice signature at all angles. The surface roughness of such level ice is generally greater than those white ice forms, while also displaying an older and deeper layered snowcover. ERS SAR backscatter values of equivalent ice floes are expected to fall in the range  $-8.8 \leq \sigma_{Ship}^o \leq -16$  dB, based on the surface scatterometer measurements, but this is heavily dependent on the physical surface characteristics.

A typical medium thick (67 cm) first-year ice sample acquired on 13 July 1992 at 65.99°S 33.53°W had interleaved bands of frazil and columnar sea-ice crystal growth, and 12 cm of layered snow. The snow-ice interface temperature was -13° C, despite air temperatures of lower than -30° C, and

the accompanying salinity at the ice surface was 14 psu. Angular depth hoar crystals developing under the, strong thermal gradient in the basal snow, contained significantly more salt than the ice surface itself, and had typical salinities of 27 psu. This highly saline, rough scattering interface at the base of the snow, probably accounts for extremely high backscatter values in the range 20-2.6° in Figure 7b. Likewise, the remainder of the snow contained significant salt content, and airborne spray from nearby leads are thought to be a contributor to the mean background level of surface snow salinity of 2 psu.

### 3.2.3.5. Rough First-Year Ice Floes

Well deformed, ridged or rubbled first-year ice floes are difficult to measure using a shipborne scatterometer, because a complete incidence angle scan is not possible from a fixed viewing position when the local topography is punctuated by piles of ice blocks. Shipborne scatterometer measurements were limited to 5 sites where surface roughness was relatively evenly distributed, and where the signature was not significantly biased by one or more features within the scan. The result is the mean signature in Figure 7c. Values of  $\sigma_{ship}^0$  are lower at near normal incidence, and fall between -11.7 and -15 dB for the SAR incidence angle band. The gradient in  $\sigma_{ship}^0$  is -0.52 dB/° in the 20-60° range, but the small sample size and averaging of individual ridges or local roughness elements cause the variability in measurement points around the logarithmic fit. Cross-polarized backscatter is greater and more variable for these rough ice floes, especially in the 20-40° range, and is explained by second-order scattering effects such as multiple scattering from blocks.

### 3.2.3.6. Multiyear Ice Floes

According to the field scatterometer data in Figure 7d, multiyear ice floes (largely second-year ice) are practically indistinguishable from rough first-year ice forms in the BRS incidence angle range. Undeformed, old floes were distinguished on the basis of snow depth, salinity and thickness as second-year ice. Mean annual thermodynamic ice growth in the absence of dynamic thickening is expected to be around 1.5 m, based on the lifecycle, mean snow depth and annual net freezing rate in the Weddell Sea [Fischer, 1995]. However, perennial ice floes observed during W WGS '92 comprised massive undeformed ice with considerable snow accumulation. Snow depths exceeding 0.75 m were commonly measured [Massom *et al.*, in Press] while ice thickness ranged from around 2 m upwards. Shipborne scatterometer  $\sigma_{ship}^0$  values from these floes fall between -12 and -15.5 dB, and the low gradient of -0.36 dB/° observed in the 30 - 50° incidence angle range, is

caused by snow volume scattering from layers and distinctive ice lenses and pipes [Massom *et al.*, In Press]. To account for volume scattering characteristics in Figure 7c, a modified 3rd order polynomial fit is applied instead of a single parameter exponential, to accommodate the flattening at 25° and rolloff beyond 55°. The distinctive feature is a plateau and higher backscatter value in the range 40-50°, and this unique may be used in 40° incidence EScat images as a method for discriminating high concentrations of thick, snow-covered perennial ice.

### 3.2.4. *Snapshot Signature Summary*

The SAR image shown in Figure 5 provides the largest mixture of ice ages and snow depths, due to its prime location in the perennial ice outflow region (Figure 1 b). The orange pdf in Figure 4 confirms a broad peak comprising a variety of pixels spanning the range of possible white, first-year and multiyear ice  $\sigma_{SAR}^0$  values. A number of samples are extracted from this image to generate Table 2. Values describe the signatures of the primary ice components, each of which is extracted on the basis of the scattering characteristics of extensive, homogeneous units of ice. Smooth and rough first-year and multi-year ice mean  $\sigma^0$  values range from -16.1 dB to -5.7 dB, in total, a further 60 samples (each of 100 or more pixels) were collected in the same manner from the SAR images shown in Figure 3, to generate a summary of snapshot winter backscatter characteristics of these primary ice types. All except the southernmost of the SAR images were acquired in regions in which W WGS '92 surface samples and ice cores were collected [Drinkwater and Haas, 1994]. Figure 8 compares and contrasts the ranges and statistics of these data with matching summary statistics inferred from the mean field scatterometer  $\sigma_{ship}^0$  curves (i.e. shaded pdf's) in Figure 7. Additional comparison data is included for open water backscatter coefficients, and MIZ scattering from brash ice or pancakes.

Inevitably, the marginal ice zone provides one of the largest ranges of backscatter signatures, due to the influence of floe size, wave environment and variable air temperature. Depending on the season and location, frazil ice growth and pancake formation may be favored. However, brash ice also provides extremely high  $\sigma^0$  values due to its similar characteristics in terms of sub-resolution floes and floe packing. A good analogy may be drawn between the Weddell and the Labrador Sea MIZ which was observed by SAR during the LIMEX experiments [Drinkwater, 1989; Livingston and Drinkwater, 1991]. In Figure 8 SAR and EScat values overlap due to the broad range in scattering conditions described in section 3.2.3.

Field sampling of smooth first-year ice floes is inherently biased, since an icebreaking ship normally seeks the path of least resistance. Although generally true, during WWGS '92 the route was largely based upon large-scale information provided by AVHRR satellite images, and it did not always enable sampling of the smoothest first-year ice. The benefit of SAR images is that they enable the very smoothest ice forms to be easily found and selected. Samples shown in Figure 8 show that the measurement ranges plotted from the shipborne scatterometer and SAR do not overlap particularly well. Similarly, with multi-year ice floes, the ship navigated around heavily ridged ice. As a consequence, the multiyear ice sampled is at the least deformed extreme of such old ice floes. Haas *et al.* (1993) document the level nature of most of the multiyear ice floes sampled. SAR backscatter values in Figure 8 indicate that the field scatterometer measurements are biased to the lower end of the MY ice range.

In terms of the signatures from the ERS scatterometer, shipborne scatterometer measurements are consistently lower at 40° incidence than equivalent INeat image data extracted in the same locations. Spatial resolution and the averaging over a number of resolution cells influences mean EScat backscatter measurements. Intervening ice motion and resulting mixtures of backscatter elements causes a relatively higher  $\sigma^0$  than that exhibited by any individual ice component. In addition, the larger roughness elements dominate the scattering in the higher incidence angle range, yet shipborne scatterometer measurements cannot easily measure the signature of such non-uniform or deformed ice floe surfaces.

Open water signatures are generated in Figure 8 for comparison, using the CMOD4 algorithm [Stoffelen *et al.*, 1993]. As expected, the range of backscatter values can, under differing wind conditions, bracket the entire range of sea-ice signatures. Nevertheless, by using image context and knowledge regarding the shape of leads within the ice pack, together with ice dynamics information from ice tracking, it is possible to distinguish open water areas within the pack. In any case, the probability of observing a lead within the Weddell Sea ice pack in winter is rare, and for the most part new leads freeze within a matter of hours after opening.

### 3.3. Seasonal Backscatter Variability

Timeseries of ERS microwave radar data demonstrate that within ice class backscatter signatures vary considerably seasonally and interannually in the Weddell Sea. The primary distinction, therefore, between seasonal and perennial ice covers can only be made by separating data acquired

during the winter ice maximum and austral summer minimum, or alternatively by continuously tracking perennial ice floes identified during the summer months, through time and space. During February and March of 1992, repeat swath SAR acquisitions were planned over Ice Station Weddell (ISW) [Gordon *et al.*, 1993]. In total 35 calibrated images were acquired over the perennial ice zone. Previously described winter SAR data acquisitions were planned during W WGS '92 in locations where RV *Polarstern* was travelling across the Weddell Sea, and in a number of other instrumented locations. The result in 1992 is a total collection of more than 55 images (exceeding  $3.5 \times 10^9$  pixels), of regions where sea-ice cover was either measured or for which independent sources of information are available. Two examples of seasonal backscatter variability are illustrated below. In the first, all IRS-1 SAR images in winter and summer states are separated and grouped, and their backscatter statistics plotted in Figure 9. In the second, in Figure 10, follow a number of ice parcels in space, to illustrate the progression in signature states [after Drinkwater and Lytle, 1996].

### .3.3.1. *Summer and Winter SAR image characteristics*

If we consider purely mid-winter and mid-summer conditions, then we may make a collection of all statistics of calibrated backscatter images on the basis of growth or melt seasons. Since the Weddell Sea ice cover is largely composed of seasonal ice, the residual ice cover at the end of summer typifies the various states of perennial ice: all ice surviving the summer melt is defined here as multi year ice. All the grouped pixel values are combined into either summer and winter pdf's in Figure 9 to describe the differences between the summer and winter perennial or annual ice signatures, respectively. The summer pdf shows a mode around -6 dB, with a small tail to higher values comprising highly deformed ice and icebergs. Ice concentrations typically exceeded 95% in the perennial ice pack and the contribution from wind-roughened open water is negligible [Drinkwater and Lytle, 1996]. At the lower end of the summer pdf is a longer tail extending to -15 dB and beyond. This includes level, undeformed multiyear ice., and snow-covered first-year ice thick enough to survive the summer melt.

In winter, the pdf becomes bi-modal with the appearance of seasonal ice. As time progresses, advection of an increasing fraction of multiyear ice northwards out of the basin reduces the probability of multiyear ice and producing the imbalanced bimodal mid-winter distribution shown in Figure 9. While a secondary peak remains, with a mode at around -7 dB, the main peak now occurs at around -12.5 dB and comprises more prevalent forms of level, first-year ice. The low end of the pdf, at values of -15 dB and below indicate the least deformed first-year ice. A winter tail extending down to the noise-floor of the SAR (-25 dB) includes small proportions of new and

young ice forms, and recent results from Jeffries and Morris (*This Issue*) in the Bellingshausen Sea indicate that typical undeformed new ice appears with a mean backscatter value of  $-23 \pm 0.5$  dB in small areas of coastal polynyas and flaw leads.

### 3.3.2. *The Summer - Autumn Transition*

Studies focusing specifically on multiyear ice in summer and winter SAR images show that its backscatter coefficient changes seasonally, and the mode of the multiyear ice pdf in Figure 9 is observed to shift slightly from around -6 dB to -7 dB between warm and cold seasons (i.e. 25% change in image scattering intensity). Surface measurements made at ISW [Lytle and Ackley, 1996] illustrate that perennial ice retains a deep snowcover on its surface. A large proportion of the ISW camp floe and surrounding ice floes experienced summer flooding at the base of the snow.

Figure 10 illustrates the temporal change of the SAR backscatter signature of tracked perennial ice floes in the vicinity of ISW as they cooled during the summer-autumn transition period. As the cold wave (i.e.  $0^{\circ}$  C isotherm) propagates downwards through the snow, areas of flooded or saturated basal snow (slush) cools and refreezes. In response to this process, C-band microwave backscatter values shown in Figure 10 decrease. [after Drinkwater and Lytle, In R&S], The period of cooling air temperatures at ISW (Figure 10a) is shown in parallel to thermistor profiles at a variety of sites with differing snow depth (Figure 10b). Thermistors indicate that protracted cold air temperatures after day 63 enable the snow layer to develop a strong thermal gradient. This cools the basal snow sufficiently quickly that the slush freezes around day 67.

Large numbers of individual multiyear ice floes were tracked in ERS-1 SAR images to derive the microwave backscatter trend shown in the upper trace of Figure 10c. For comparison global SAR-image backscatter means and EScat  $\sigma^0$  values, measured over the identical  $100 \times 100$  km SAR-imaged areas, each report essentially the same decreasing trend. The largest decrease in  $\sigma^0$  is observed before and after the freeze-up of the slush. Thus, the change from rough surface scattering from snow-covered slush to rough surface scattering from dry snow-covered perennial ice appears responsible for the observed shift in the multiyear ice peak in Figure 9. Indeed, the mean values of

### 3.3.3. *Meltponding*

Additional effects of transformation at the surface of perennial ice floes occur as a consequence of summer melt processes and periodic winter excursions in air temperature due to storm systems [Massom *et al.*, In Press]. Large excursions in air temperature have been observed to have considerable impact upon the microwave backscattering characteristics of sea ice, in response to the changing surface snow and ice characteristics [Drinkwater *et al.*, 1995a]. Meltponds have commonly been observed near to the ice margin during shipborne experiments [Haas *et al.*, 1992]. Though the appearance of classical meltponds in the Weddell Sea appears to be checked by the latitudinal limit of southward penetration of the zero degree isotherm, recent studies have recorded observations of surface meltponding of perennial ice floes further to the south in the Weddell Sea [Low, 1995]. The appearance and expression of meltponding in SAR images is discussed in further detail in this issue by Low and Wadhams.

## 4. **Weddell Sea Ice Dynamics**

Studies by Vichoff and Li (1995), Vihma *et al.* (1996) and Kottmeier and Sellmann (1996) have pieced Lagrangian buoy drift statistics together to reconstruct the seasonal and regional patterns of ice drift in the Western Weddell Sea in response to winds and currents. Recent work by Drinkwater and Kottmeier, (1994) introduced ice-motion tracking from mesoscale SAR data as an alternative method for deriving kinematic measurements of the Weddell ice cover. In contrast to the Arctic ice motion studies using ERSSAR [Kwok *et al.*, 1990], the capability to track Antarctic ice using automated SAR motion tracking of had not been demonstrated. The reason was because in the Arctic, large fractions of multiyear ice provide high contrast targets which can be successfully tracked in time using radar images. Weddell Sea ice in comparison exhibits large expanses of low contrast, level first-year ice, and a lack of distinct features with which computer algorithms may successfully track the ice.

### **4.1. Tracking Ice Station Weddell**

As previously described in section 2, a series of SAR image acquisitions were planned in conjunction with the 1992 drift of ISW. Figure 11 [after Drinkwater, *In Prep.*] indicates a result from tracking snow-covered perennial ice floes (in the vicinity of ISW - marked by +), during the early drift phase of the experiment (February - March 1992). Two overlapping images acquired along 1-day spaced crossing orbits (during the so-called "Ice Phase" orbit of ERS-1) were correlated to produce the displacement vectors using the algorithm described by Kwok *et al.*

(1990). Figure 11 shows the 5 km gridded ice drift displacement field superimposed on the ERS-1 SAR reference image (orbit 3058 frame 5103), acquired at 11:34 GMT on 15 February, 1992 at 71.59° S 53.04° W. Spots indicate the gridded starting positions of tracked features, and the scaled vector arrows indicate the distance traveled in the 17h period separating the two images. Vectors imply strong cyclonic motion, and mean and standard deviations of the  $u$  and  $v$  velocity components are  $-10.432 \pm 2.5$  and  $5.95 \pm 2.7$   $\text{cm s}^{-1}$ , respectively. Partial derivatives of velocity over the entire tracked portion of the scene indicate a mean divergence of  $0.15 \pm 0.63$   $\% \text{ d}^{-1}$ ; a mean vorticity of  $-0.45 \pm 0.70$   $\% \text{ d}^{-1}$ ; and mean shear of  $2.01 \pm 1.02$   $\% \text{ d}^{-1}$ .

#### 4.1.1. GPS Validation of Ice Velocity

*The* period of consecutive ERS-1 SAR imaging of the ISW camp floe lasted between day 38 (7 Feb) through day 75 (15 Mar), in 1992. Initial results, such as Figure 11, demonstrate that algorithms developed for the winter Arctic can be used without serious problems in both cases of ISW summer perennial ice or relatively featureless smooth Weddell Sea winter first-year ice. In order to establish the success and accuracy of the tracking algorithms, positions from a fixed GPS receiver at the ISW camp are compared with SAR ice-tracked drift vectors. GPS positional fixes were not logged until after day 57, preventing accurate interpolation of latitude and longitude positions of the camp earlier than this date. The period of highest frequency GPS measurements overlaps with 6 consecutive SAR ice velocity image “pairs” (i.e. 12 consecutive images), allowing comparisons to be made between day 57 and 75. Figure 12 shows the correlation between mean velocity components derived from SAR (such as that in Figure 11) and those derived from instantaneous GPS ISW locations (interpolated to the exact SAR imaging times). SAR  $u$  and  $v$  velocity components are rotated into the local coordinate system to match calculated GPS velocities.

In terms of different mean ice drift speeds Figure 13 indicates a sample ranging from 2-10  $\text{cm s}^{-1}$ . Figure 12a shows the west-east (i.e.  $x$  or  $u$  component) and 12b south-north (i.e.  $y$  or  $v$ ) components of velocity, while 12c indicates the magnitude of the velocity. Ice drift is largely westward and northward during this period. Although a small sample, the plot shows a high degree of accuracy in deriving both the direction and magnitude of ice drift. Although spatial mean SAR velocities are used in the regression analysis, as opposed to values of the SAR-derived velocity interpolated to the ISW floe location, the result in 12c indicates a correlation of 0.98 (illustrated by the dotted regression line). The error in SAR motion tracking is computed to be less than 0.5  $\text{cm s}^{-1}$  for 3-day motion tracking. This translates into an error of -100m, or equivalently -1 pixel



after accounting for error variance generated by temporal interpolation of GPS locations and spatially averaged mean SAR velocity vectors,

The largest outlying vector in Figure 13 is identified throughout by a curly arrow, indicating that the motion field displays a large amount of rotation or vorticity. As Figure 11 graphically shows, the mean velocity components of such a field are not sufficiently representative of any single point in space for a good comparison to be made. On the other hand, it is felt that spatial interpolation of velocity field is unrepresentative of true inter-particle floe motions, and so a further comparison was not made to try to improve this result.

#### 4.1.2. *Ice Kinematics Timeseries*

Results of processing all 3-day or 1-day repeat overlapping “pairs” into ice kinematics information are shown as a velocity timeseries in Figure 13 together with surface wind speed and the GPS monitored drift of the ISW camp floe. In Figure 13(a) ISW measurements of the wind speed are shown as a dotted line. Prior to completion of the meteorological mast on day 57 once or twice daily windspeeds were recorded. The overlapping solid line indicates the ECMWF daily mean analysis field surface wind speed prior to day 57, whereafter the solid line is a 3-day running mean of the hourly means recorded by the ISW met station anemometer.

Figure 12 (b) and (c) show the mean SAR instantaneous velocity components joined by a dotted trend line. Horizontal bars indicate the period separating the tracked image pair, and the vertical bar indicates one standard deviation ( $1\sigma$ ) about the mean velocity vector (spatially averaged over a 100 x 100 km scene). An overlapping solid line indicates the 3-day smoothed velocity of ISW and begins upon installation of a fully functional GPS at ISW (on day 57). Hollow diamond symbols represent the velocity computed from distances traveled between instantaneous GPS locational “fixes”, between SAR imaging times. Where diamonds overlap mean SAR velocity measurements, the spatially averaged SAR velocity is representative of a single GPS velocity vector. In a spatial context, where the mesoscale velocity field does not represent translational motion, the ISW GPS velocity diamond does not overlap the mean SAR velocity. Thus, in the case of day 70 the discrepancy shown in Figure 13(b) and (c) is explained by strong anticyclonic or cyclonic motion, and is similar to the example in Figure 11. A mean velocity of a spatial field of cyclonic or anticyclonic flow is unrepresentative of any single vector within that field, and such means cannot be directly compared to the GPS ISW velocity. Nevertheless, smoothed 3-day velocity components respond to sustained bursts of wind shown in the solid line in Figure 13(a). Additionally, though

not in pure "free-drift", the SAR-reported drift velocity components (dotted line in (b) and (c)) clearly respond to the 3-day filtered wind forcing. The largest discrepancy between SAR velocity and 3-day smoothed ISW velocity occurs as a result of the wind burst from day 63 to 67, when ISW is pushed to the west at -15 ems-l. In the corresponding SAR image record the closest pair of image acquisitions was 6-days, and thus the minimum in u velocity is missed. A higher temporal resolution in SAR imaging is required to capture such deviations in ice motion.

Generally, examples such as Figure 13 indicate that the sea-ice drift field for the most part responds swiftly to the synoptic pressure-field driven geostrophic winds. The temporal frequency of fluctuations in the field of ice velocity vectors closely match those in wind velocity. Temporal spacing of less than 3-d sampling is concluded necessary if the small-scale response to synoptic storms is to be studied in more detail in an open basin such as the Weddell Sea. In addition, 1-day repeat orbits, plotted at day 46, 52, and 71 curiously capture more variance in ice velocity. Preliminary spectral studies using buoy data confirm this phenomena to be attributable to the aliasing of velocity components induced by tidal motions [Drinkwater, *In l'rep*]. Importantly, therefore, exact 3-day repeat orbits do not alias diurnal or semi-diurnal (which are close to 12 hr. period) tidal motions, whereas non-multiples of 12 hours contain significant tidal variance in this location. Ultimately, a trade-off is ultimately necessary between resolution in temporal sampling and the sampling interval over which ice floes are tracked. The best solution appears to be 3-day SAR ice-motion tracking at regular one day intervals, but issues such as the SAR data volumes (for required coverage of the entire Weddell Sea) become paramount, Radarsat ScanSAR image coverage may be the only future high-resolution SAR solution.

#### **4.2. Rheological Response**

The ultimate scientific goal of employing automatically-generated SAR ice kinematics products is to develop a spatial and temporal picture of Weddell Sea ice drift and opening and closing of the ice in response to various components of the momentum balance. Fig. 14 illustrates a product derived from the SAR ice velocity field in Fig. 11. The ice deformation is defined in terms of the ratio of strain-rate invariants, themselves calculated from velocity derivatives from the 5 km grid. The angle of change,  $\theta = \tan^{-1} F_{II}/E_I$  expresses the style of deformation, where a positive  $E_I$  represents divergence (negative = convergence) and  $F_{II}$  the rate of shearing. The result is a graphical illustration of whether the motion is accompanied by either predominantly divergence (i.e.  $\theta = 0$ ), shear ( $\theta = 90^\circ$ ), or convergence ( $\theta = 180^\circ$ ). We note for the field of cyclonic motion recorded in Fig. 11, that a large proportion of the deformation represents shear-style motion (indicated by dark blue and pink). A single purple 5 km grid cell located to the north-west of the ice camp (marked by

+) illustrates a situation tending towards pure convergence. It clearly begins as an area of small ice floes, with a large fraction of open water. Such sea-ice deformation data can be used in validating ice rheologies presently employed in coupled ice-ocean-atmosphere models [Stern *et al.*, 1995]. More accurately parametrized coupled regional ocean-ice-atmosphere models together with SAR data will be used to evaluate the relationship between the changing basin-wide distribution of sea ice and the momentum flux [Drinkwater *et al.*, 1995b]. Accurate monitoring of Weddell Sea ice formation, drift, deformation and divergence are also of primary importance to estimating surface fluxes of heat, freshwater and salt [Drinkwater *et al.*, 1995c].

#### 4.3. Synoptic Scale Motion Tracking

Updated tracking schemes are presently being tested with ERSAT images to derive a large-scale motion fields at a reduced resolution. Figure 15 shows a preliminary example of an Antarctic ice motion climatology where 3-day mean ice motion vectors are overlaid onto an ERS-1 scatterometer A image (i.e. 40° incidence angle) centered on day 255, 1992. Arrows indicate an unfiltered, weighted average of all motion vectors, derived from over 100 ice motion products generated from pairs of 1992 ERSAT images at 3-day intervals. Locations where seasonal ice does not appear year-round (i.e. less tracked vectors), have less reliable statistics and are noisier.

Although further work is required to validate these products, details of the Weddell sea-ice circulation are clearly highlighted in Figure 15 on a 100 km grid. The details of the northward drift in the Western Weddell Sea are recognized, as is the north-westward motion away from the coastal regions in the eastern Weddell Sea. Changes in patterns observed in the backscatter images in section 3.1 are more easily explained once dynamic information such as this become available. Future comparisons will be made between individual ERSAT ice motion products and buoy drift trajectories, and other climatologies constructed from historical buoy drift datasets [Kottmeier and Sellmann, 1996].

## 5. Conclusions

Sea-ice conditions in the southwestern Weddell Sea are analysed using available satellite- and ship-borne microwave radar remote sensing techniques. In particular, the temporal and spatial variability in seasonal and perennial ice are identified in ERS SAR and Scatterometer data. Variability is described in terms of both the microwave radar response to changing surface conditions and sea-ice dynamics. It is shown that large-scale ice patterns observed using C-band satellite radar

progressively change as a function of the ice-growth season and the residual amount of perennial ice in the Weddell Sea. Resolution-dependent microwave signatures of individual components of the ice cover are identified which may be used as markers in the microwave data record. Furthermore, the complementary nature of the high resolution SAR and Scatterometer data is exploited to highlight these characteristics in the context of both snapshot and timeseries records.

Combinations of microwave data sources, together with ground based data, indicate the southwestern Weddell Sea comprises a number of distinct sea-ice regimes. A number of large icebergs which have been grounded off Berkner island in much the same location over the early part of this decade have markedly altered the dynamics and character of the sea ice, especially in the south-western part of the basin. Being starved of deformed ice, this region is different from the remaining winter ice conditions. To-date, during the 1990's it appears to have been composed primarily of first-year ice. Temporary polynyas forced by katabatic winds off the Ronne Ice Shelf in this location, might be considered as main ice formation source for the south-western continental shelf region. The spatial separation of this and other regimes is correlated with the continental slope, indicating that the barotropic part of the Weddell Gyre ocean circulation, together with the synoptic pressure pattern, are dominant factors responsible for the forcing of the ice cover in the remainder of the basin. Perennial ice formed to the east of the grounded icebergs, meanders its way northwards before being ejected eastwards out of the basin. It appears to closely follow climatological drift streamlines and bottom topography. Old, deformed ice, originating in the vicinity of the grounded icebergs, becomes separated from perennial ice forming on the shelf along the Antarctic peninsula by a northwards, seasonally-propagating shear line at around 54°W. The location of this shear line is oriented approximately along the 2000m isobath, and defines the margin of more slowly moving ice to the west. ERS data indicate that areas of increased compactness and ice deformation may be found in this northwestern part of the Weddell Sea, especially off the Larsen Ice Shelf. In contrast, the central part of the Gyre, defined from the ice-motion climatology as approximately 67°S 20°W, experiences divergent drift and formation of largely undeformed, level first-year ice. Laser profiling from RV *Polarstern* during WWGS '92 confirms central Weddell Sea ice to have a much lower ridging density than encountered on both the westernmost or easternmost flanks of the basin [Dierking, 1995].

Despite some problems experienced in tracking the more dynamic ice margins during periods of maximum ice extent, ice-motion tracking using ERSAT images appears to be a promising addition to SAR and AVHRR ice-floe tracking. Large-scale ice tracking methods promise to fill in missing

information about basin-wide drift conditions, especially during periods without buoy drift campaigns, or between SAR imaging or cloud-free AVHRR overpasses. More detailed analysis of ice dynamics data must now be made in conjunction with timeseries of ERS images to prove various hypotheses about the connection between deformed ice, high backscatter regions and convergent flow, or *vice-versa* between level ice, low backscatter and divergent flow. Present 1 y, motion data are being compared in a quantitative fashion with results of theoretical sea ice models of the Weddell Sea [e.g. Drinkwater *et al.*, 1995b] to improve our understanding of the ice dynamics contributing to observed patterns. Now ice-tracking techniques have been successfully tested and applied on both SAR and Scatterometer images from the Weddell Sea, a detailed historical ice-motion database can be built up. The response of the sea ice to synoptic-scale variations in the momentum balance can be more effectively studied using these data. Similarly, information provided on the rheological and dynamical response of the ice cover will benefit the latest generation of Weddell Sea ice models.

In this paper, examples indicate that microwave radar images obtained by satellites such as ERS and RADARSAT will revolutionize our understanding of sea-ice processes in Antarctica. Though limitations still exist on the reception of SAR data, enhanced-resolution scatterometer images have been shown to provide an essential complement. The advantage of Scatterometer images, in contrast to SAR or 25km resolution passive microwave images is that they trace and highlight large-scale ice characteristics, directly resulting from dynamical processes. The recent successful launch of the ADEOS satellite, together with the Ku-band NASA Scatterometer (NSCAT) instrument, will ensure future uninterrupted production of full polar images at an even higher resolution. Various improvements can be made over the present ERSat image processing, due to the additional Doppler information provided in the NSCAT datastream. Backscatter cell location is more precisely known, and consequently NSCAT enhanced resolution images will likely double that presently achieved using ERS scatterometer data. Furthermore, the NSCAT instrument traces swaths on both sides of the spacecraft, effectively doubling the amount of coverage achieved on a daily basis. This implies that a higher temporal resolution may be derived from NSCAT for use in ice motion tracking. Future plans include implementing ice motion tracking over the entire north and south polar regions when NSCAT becomes operational.

## 6. Acknowledgments

Enhanced resolution ERS-1 scatterometer data were kindly processed by David Long and David Early of BYU for this study, as part of a joint European Space Agency supported A02.IJSA.119

project. SAR data are processed and supplied by the German Processing and Archiving Facility, and especial thanks go to Jörg Gredel and Birgit Schättler. Ron Kwok and Shirley Pang are thanked for generating ice motion products from EScat images. MRD performed this work at the Jet Propulsion Laboratory, California Institute of Technology under contract to NASA, and the kind support of Robert H. Thomas of Code YSG, NASA.

## 7. References

Augstein, E., N. Bagriantsev, and H.W. Schenke. (Eds.), 1991, The Expedition Antarktis VIII/1 - 2, 1989 with the Winter Weddell Gyre Study of the Research Vessels "Polarstern" and Akademik Fedorov. *Reports of Polar Research*, 84, Alfred-Wegener-Institut für Polar- und Meeresforschung, Bremerhaven, Germany, 134pp.

Bally, P., K. Fellah, Evaluation of the Accuracy of the Backscattering Coefficient Measurement in SAR Data Products, *ESA/ESTEC Earth Sciences Division Technical Note*, July 1995.

Brennecke, W., Die Ozeanographischen Arbeiten der Deutschen Antarktischen Expedition 1911-1912, *Aus den Archiven Deutsche Seewarte*, 34, 195, 1921.

Dierking, W., Laser profiling of the ice surface topography during the Winter Weddell Gyre Study 1992, *J. Geophys. Res.*, 100, C3, 4807-4820, 1995

Drinkwater, M. R., The drift of Ice Station Weddell, *J. Geophys. Res.*, In Preparation.

Drinkwater, M. R., Satellite Microwave Radar Observations of Antarctic Sea Ice. In C. Tsatsoulis and R. Kwok (Eds.), *Recent Advances in the Analysis of SAR for Remote Sensing of the Polar Oceans*, In Press,

Drinkwater, M. R. (Ed.), PIPOR Special Issue, *Int. J. Remote Sens.*, 16, 17, 1995.

Drinkwater, M. R., LIMEX '87 Ice surface characteristics; implications for C-band SAR backscatter signatures. *IEEE Transactions on Geoscience and Remote Sensing*, 27, 5, 501-513, 1989.

Drinkwater, M. R., and V.I. Lytle, ERS-1 SAR and Field-Observed Characteristics of Austral Fall Freeze-up in the Weddell Sea, Antarctica, *J. Geophys. Res.*, In Press.

Drinkwater, M. R., and C. Kottmeier, Satellite Microwave Radar- and Buoy-tracked Ice Motion in the Weddell Sea during WWGS '92. *Proc. IGARSS '94*, 1, Pasadena, CA, Aug. 8-12, IEEE Cat, No. 94 CH3378-7, 153-155, 1994.

Drinkwater, M. R., and C. Haas, Snow, Sea-Ice and Radar Observations during ANT X/4: Summary Data Report, *Berichte aus dem Fachbereich Physik*, 53, Alfred Wegener Institut für Polar- und Meeresforschung, Bremerhaven, Germany, 58 pp., 1994.

Drinkwater, M. R., D.G. Long, and D.S. Early, Enhanced Resolution Scatterometer imaging of Southern Ocean Sea Ice, *ESA Journal*, 17, 307-322, 1993a.

Drinkwater, M. R., Hosseinmostafa, R., and W. Dierking C-band Microwave Backscatter of Sea Ice in the Weddell Sea during the Winter of 1992. *Proc. IGARSS '93*, Tokyo, Japan, Aug. 18-21, Vol. 2, 446-448, 1993b.

Drinkwater, M. R., D.S. Early and D.G. Long, ERS - 1 Investigations of Southern Ocean Sea-Ice Geophysics using Combined Scatterometer and SAR Images. *Pmt. IGARSS '94*, Vol. 1, 165-168, Pasadena, CA, Aug. 8-12, IEEE Cat. No. 94CH3378-7, 1994.

Drinkwater, M.R., R. Hosseinmostafa, and S.P. Gogincni, C-band Backscatter Measurements of Winter Sea Ice in the Weddell Sea, Antarctica, *Int. J. Remote Sensing*, 16, 17, 3365-3389, 1995a.

Drinkwater, M. R., H. Fischer, M. Kreyscher, and M. Harder, Comparison of Seasonal Sea-ice Model Results with Satellite Microwave Data in the Weddell Sea, *Pmt. IGARSS '95*, Vol. 1, Florence, Italy, 10-14 July, IEEE Cat. No. 95CH35770, 357-359, 1995b.

Drinkwater, M. R., D.G. Long, and D.S. Early, Comparison of Variations in Sea-ice Formation in the Weddell Sea with Seasonal Bottom-Water outflow Data. *Proc. IGARSS '95*, Vol. 1, Florence, Italy, 10-14 July, IEEE Cat. No. 95CH35770, 402-404, 1995c.

Early, D.S., and D.G. Long, Azimuth Modulation of C-band Scatterometer so Over Southern Ocean Sea Ice, Accepted for Publication in *IEEE Transactions on Geoscience and Remote Sensing*, 1996.

ESA Earthnet, ERS- 1 System, *ESA Special Publication*, SP- 1146, ESA Publications Division, ESTEC, Noordwijk, The Netherlands, 87 pp., 1992.

Jahrbach, E., G. Rohardt, M. Schröder, and V. Strass, Transport and structure of the Weddell Gyre, *Ann. Geophys.*, 12, 840-855, 1994.

Fischer, H., Comparison of an optimised dynamic-thermodynamic sea-ice model with observations in the Weddell Sea, *Reports on Polar Research*, 166, Alfred-Wegener-Institut für Polar- und Meeresforschung, Bremerhaven, Germany, 130pp.

Gohin, F., Some Active and Passive Microwave Signatures of Antarctic Sea Ice from Mid-Winter to Spring 1991, *Int. J. Remote Sens.*, 16, 11, 2031-2054.

Hosseinmostafa, A.R., V.J. Lytle, K.C. Jezek, S.P. Gogineni, S.F. Ackley, and R.K. Moore, Comparison of radar backscatter from Antarctic and Arctic sea ice, *Electromag. Wave Applications*, 9, 421-438, 1995.

ICC Station Weddell Group, Weddell Sea Exploration from ICC Station, *EOS*, 74, 11, 121 and 124-126, 1993.

Kottmeier, C., and L. Sellmann, Atmospheric and Oceanic Forcing of Weddell Sea Ice Motion, Submitted to *J. Geophys. Res.*, In Press.

Kwok, R., J.C. Curlander, R. McConnell, and S.S. Pang, An ice-motion tracking system at the Alaska SAR Facility, *IEEE J. Oceanic Eng.*, OE-15, 1, 44-54, 1990.

Laur, H., P.J. Meadows, J.J. Sanchez, and E. Dwyer, ERS - 1 SAR Radiometric Calibration, Proc. of the CEOS SAR Calibration Workshop, ESTEC, Noordwijk, Netherlands, *ESA Pub, WPP-048*, 257-281, 1993.

Lemke, P. (ed.), 1994, The Expedition ANTARKTIS X/4 of RV "Polarstern" in 1992, *Reports on Polar Research*, 140, Alfred-Wegener-Institut für Polar- und Meeresforschung, Bremerhaven, Germany, 90pp.

Long, D.G., P.J. Hardin, and P.T. Whiting. Resolution Enhancement of Spaceborne Scatterometer Data. *IEEE Trans. Geosci. Remote Sensing*, 31, 3, 700-715, 1993.

Low, D., The Validation of ERS-1 Summer SAR Data for Antarctic Summer Sea Ice, *Unpublished M. Sc. Thesis*, 143pp., 1995.

Lytke, V., and S. Ackley, Heat Flux through Sea Ice in the Western Weddell Sea: Convective and Conductive Transfer Processes, *J. Geophys. Res.*, 101, C4, 8853-8868, 1996.

Lytke, V. J., K.C. Jezek, S.P. Gogineni, and A.R. Hosseinmostafa, Field Observations of Microwave Backscatter from Weddell Sea Ice, *Int. J. Remote. Sens.*, 17, 1, 167-180, 1996.

Massom, R. A., Observing the Advection of Sea Ice in the Weddell Sea using Buoy and Satellite Passive Microwave Data, *J. Geophys. Res.*, 97, C10, 15559-15572, 1992.

Massom, M., M.R. Drinkwater and C. Haas, Spatial and Temporal Distribution of Winter Snowcover Properties on Sea Ice in the Weddell Sea, *J. Geophys. Res.*, In Press.

Morris, K. and M.O. Jeffries, Sea ice characteristics and seasonal variability of ERS-1 SAR backscatter in the Bellingshausen Sea, *AGU Antarctic Series*, This Issue.

Muench, R.D., and A.L. Gordon, Circulation and Transport of Water along the western Weddell Sea, *J. Geophys. Res.*, 100, C9, 18503-18515, 1995.

NSIDC, DMSP SSM/I brightness temperature and sea ice concentration grids for the Polar regions on CD-ROM, Users guide. National Snow and Ice Data Center Special Report, 1, Boulder, CO, USA., ??pp.

Orsi, A.J., W.D. Nowlin, Jr., and T. Whitworth 111, On the circulation and stratification of the Weddell Gyre, *Deep Sea Res.*, 40, 169-203, 1993.

Stern, H. L., D.A. Rothrock, and R. Kwok, Open water production in Arctic sea ice: Satellite measurements and model parameterizations, *J. Geophys. Res.*, 100, C10, 20601-20612, 1995.

Schnack-Schiel, S. (Ed.), 1987, The Winter Expedition of RV "Polarstern" to the Antarctic (Ant V/1-3). *Reports on Polar Research*, 39, Alfred-Wegener-Institut für Polar- und Meeresforschung, D-27568, Germany, 259pp.

Stoffelen, A., and D.L.T. Anderson, IRS-1 Scatterometer Data Characteristics and Wind Retrieval Skill, Space at the Service of Our Environment, *Proc. 1st ERS-1 Symp.*, 4-6 Nov. 1992, Cannes, France, *ESA SP-359*, Vol. 1, 41-47, 1993.



Viehoff, T., and A. Li, Iceberg Observations and Estimation of Submarine Ridges in the Western Weddell Sea, *Int. J. Remote Sens.*, 16, 17, 3391-3408, 1995.

Viehoff, T., A. Li, C. Oelke, and H. Rebhan, Characteristics of winter sea-ice conditions in the southern Weddell Sea in 1992 as derived from multi-sensor observations. *Proc. IGARSS '94*, Pasadena, California, USA, Aug. 8-12, Vol. 1, 150-152, 1994.

Vihma, T., J. Launiainen, and J. Uotila, Weddell Sea ice. Drift: Kinematics and Wind Forcing, *J. Geophys. Res.*, 100, C9, 18503,18515, 1995.

Zibordi, G. and M.L. Van Wocrt, *Remote Sensing of the Environment*, 45, 155-163, 1993.

## 8. Figures

Figure 1. Weekly mean SIRF A image in the ERS-1 Scatterometer mode, for (a) February 26 (i.e. days 54-61), 1992; and (b) 31 July (i.e. days 210 - 216), 1992. ERS-1 Scatterometer data © ESA.

Figure 2. Weddell Sea time-series of weekly EScat A images, illustrating evolving backscatter characteristics of the sea-ice cover from minimum to maximum ice extent in 1992. Day of Year periods illustrated are; (a) 32-38; (b) 53-59; (c) 74-80; (d) 104-110; (e) 125-131; (f) 146-152; (g) 167-173; (h) 188-194. Coastlines and ice shelves are indicated by a thin white line while the Joint-ICC Center sea-ice margin is identified by a thick line. ERS-1 Scatterometer data © ESA.

Figure 3. Map indicating ERS-1 SAR image frames used in regional backscatter analysis (see Table 1).

Figure 4. SAR backscatter pdf's for each individual scenes (in six colors), and for the entire grouped winter SAR dataset (see Figure 3. and Table 1 for SAR scenes) in black.

Figure 5. ERS-1 SAR image from orbit 5249, frame 4941, taken on 17 July, 1992 [©ESA, 1992] and located in Figure 3. Boxes highlight regions from which component backscatter distributions are plotted in section 4.2.2. The inset marks the location of the image with respect to the track location of the research icebreaker Polarstern.

Figure 6. (a) Photograph pancake ice field on 13 June, 1992; (b) sea-ice sample at this location at site N04 1501; and (c) shipborne scatterometer scan at this site location, together with contrasting scan from 14 June and EScat A measurement in the same location.

Figure 7. Mean WWGS '92 shipborne scatterometer ice signatures, from (a) white ice, (b) smooth first-year ice; (c) rough first-year ice; and (d) multiyear ice. Curves are fitted exponentially and error bars indicate the standard error of the data. Vertical lines delineate the incidence angle range of ERS SAR ( $20 \leq \theta < 26^\circ$ ) and overlapping shaded pdf's show the probability distribution from SAR pixel samples in the locations of shipborne scatterometer measurements. A range of observed SAR values is shown for all sampled images for each ice type.

Figure 8. Summary plot of C-band Weddell Sea ice and ocean signatures, indicating the ranges and/or standard deviation of SAR, and shipborne or EScat backscatter measurements of each broad ice category.

Figure 9. Seasonal SAR backscatter probability distribution functions. Bimodal peaks in winter distribution comprise first-year or seasonal (FY), and multiyear (MY) or perennial ice.

Figure 10. Timeseries of (a) surface air temperatures from the Finnish Salargos buoy; (b) snow-temperature gradients at thermistor sites on snow-covered perennial ice floes; (c) ■ or  $\bar{\sigma}_{SY}^o$  Of multi year floes (vertical bars indicating range of values), x or (i.e. global SAR image means), and  $\bar{\sigma}_{Scat}^o$  or  $40^\circ$  incidence normalized backscatter coefficient; (d) ♦ - EScat backscatter gradient  $M$  (linear regressed) at  $40^\circ$  incidence.

Figure 11. 3-day ice motion vectors superimposed onto an ERS-1 SAR image for 15 March 1992 [Image ©ESA, 1992]. A scale indicates the distance (in km) of the vector displacements and the mean u and v components of ice velocity and given at upper left,

Figure 12. Comparison of SAR-tracked 3-day velocities with equivalent 3-day velocities computed from instantaneous GPS locations of Ice Station Weddell.

Figure 13. Timeseries of ERS-1 SAR-tracked ISW ice motion results. (a) shows measured surface windspeed (dotted) and 3-d smoothed wind speed; (b) shows SAR (dotted) and GPS-derived (solid) u component of velocity (i.e. west is positive); (c) v components of velocity (north positive) from SAR (dotted) and GPS (solid - 3-d running mean).

Figure 14. Color-coded display of deformation angle  $\theta$  (i.e.  $\tan^{-1}(E_{II}/E_I)$ ).

Figure 15. Preliminary EScat ice motion climatology, constructed from an unweighted average of ice motion grids generated at 3-d intervals throughout 1992.

## 9. Tables

Table 1. List of FIRS- 1 SAR image frames used in regional backscatter data analysis.

image (orbit/frame)	Date and Time (UTC)	Center Latitude	Center Longitude
50905121	6 July 92:09:01:35.786	-72.263	343.424
52494941	17 July 92:11:34:19.254	-64.706	318.550
53775031	26 July 92:10:12:16.392	-68.614	333.541
53875949	27 July 92:03:11:05.712	-60.406	310.928
53875967	27 July 92:03:11:20.807	-59.581	310.165
54495139	31 July 92: 10:56:54.090	-72.934	312.629

Table 2. Summary of backscatter samples from ERS-1 SAR image 5249/4941 in Figure 5.

Ice Type	Sample #	Mean/Median (dB)	Std. Deviation (dB)
Smooth First-Year	FYS 1	-16.09/-16.10	$\pm 0.99$
	FYS 2	-15.46/-15.50	$\pm 1.05$
Rough First-Year	FYR 1	-10.14/-10.30	$\pm 1.83$
	FYR 2	-9.54 /-9.5	$\pm 1.69$
Multiyear Ice	MY 1	-5.72/-5.50	$\pm 1.88$
	MY 2	-6.81/-6.50	$\pm 2.27$
	MY 3	-5.97/-5.50	$\pm 2.03$

Table 3. Summary of winter C-band EScat backscatter ranges ( $\theta = 40^\circ$  incidence) of main categories of sea ice in the Weddell Sea.

Ice Type	Backscatter Range
Icebergs	$-6.0 \leq \sigma^0 \leq 0.0$
Multi year/Pancakes	$-11.0 \leq \sigma^0 < -6.0$
Rough First-year	$-14.0 \leq \sigma^0 < -11.0$
Smooth First-year	$-20.0 \leq \sigma^0 < -14.0$
Nilas	$-32.0 \leq \sigma^0 < -20.0$

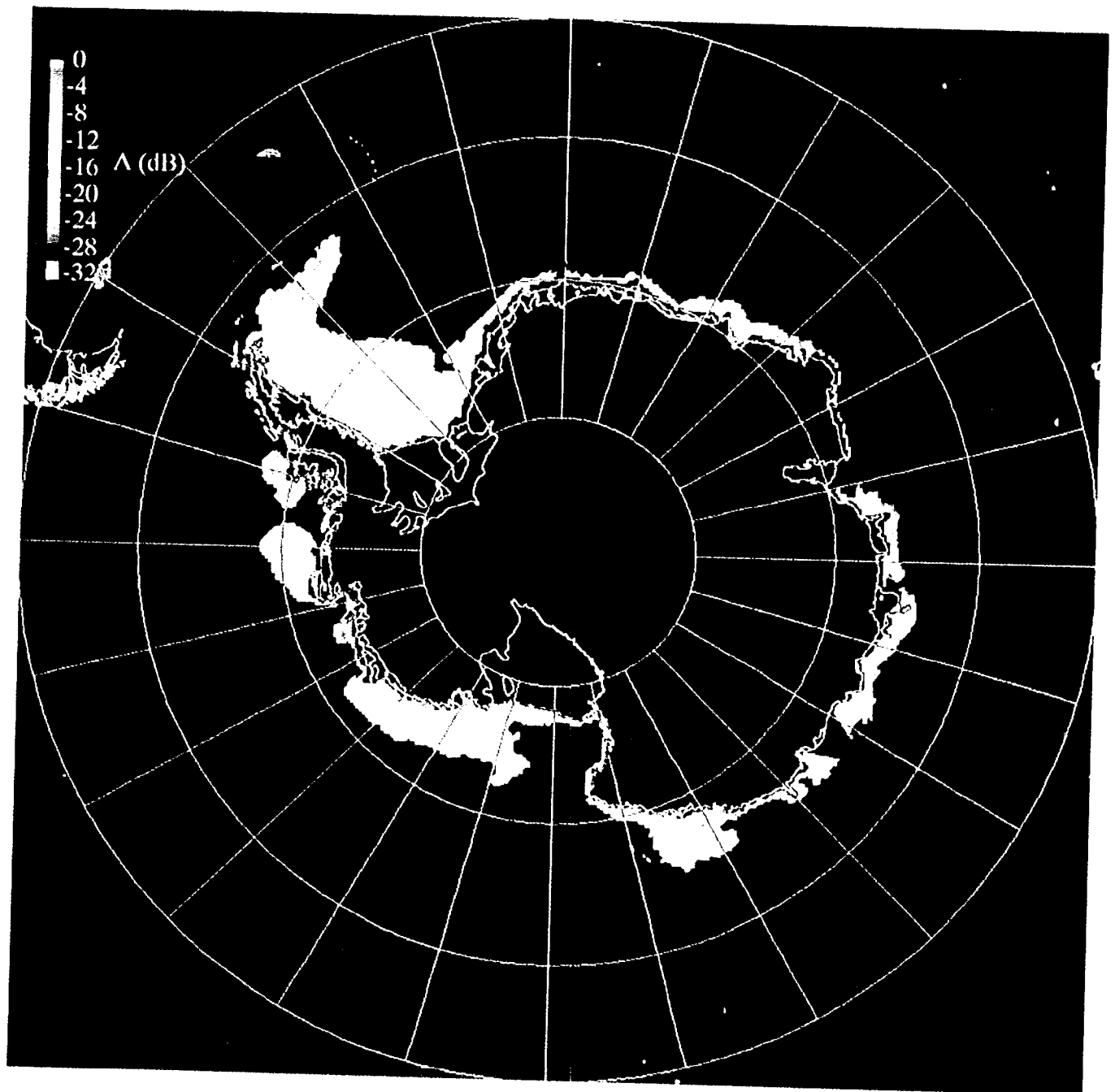


FIGURE 1a

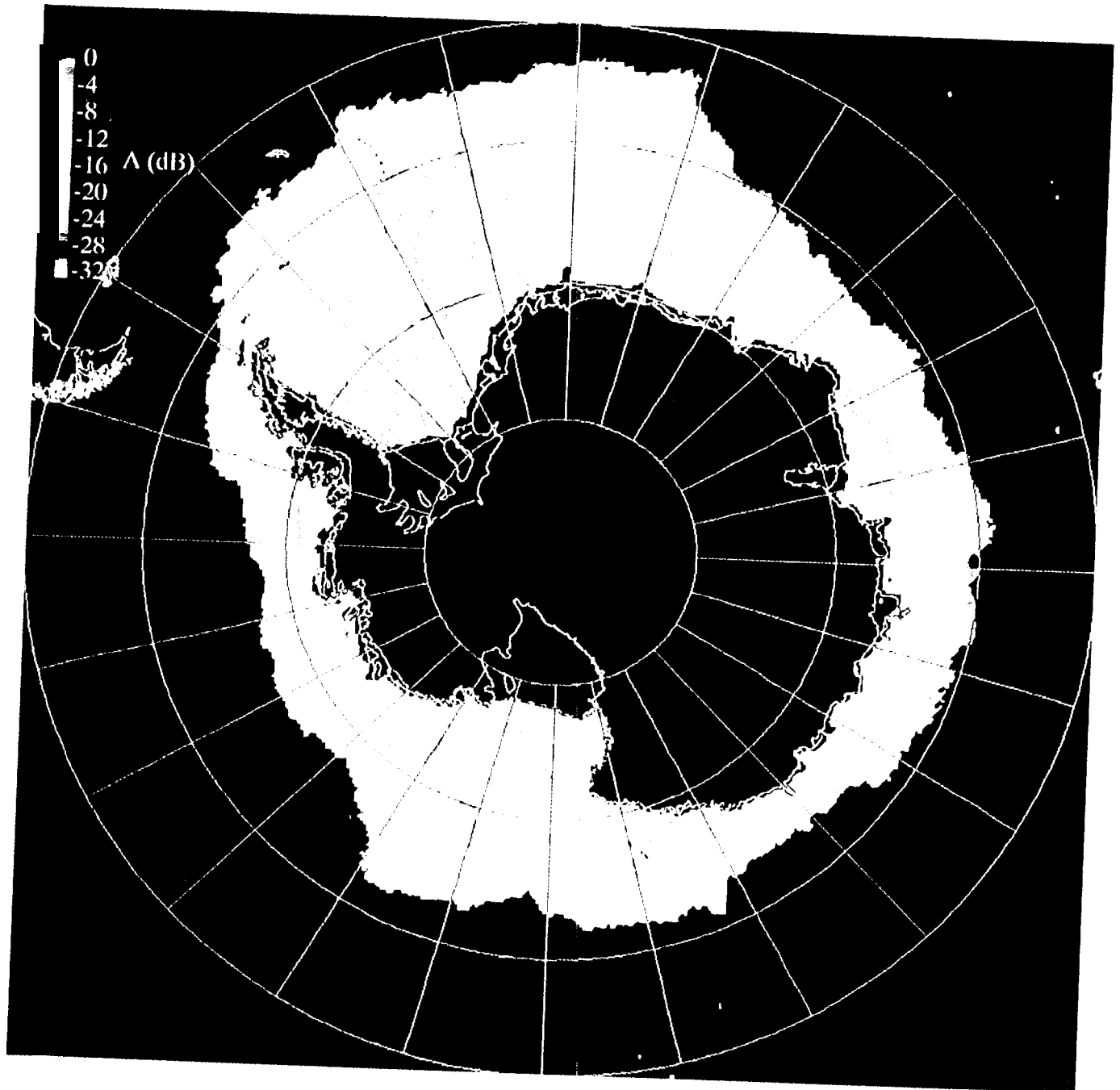


FIGURE 1b

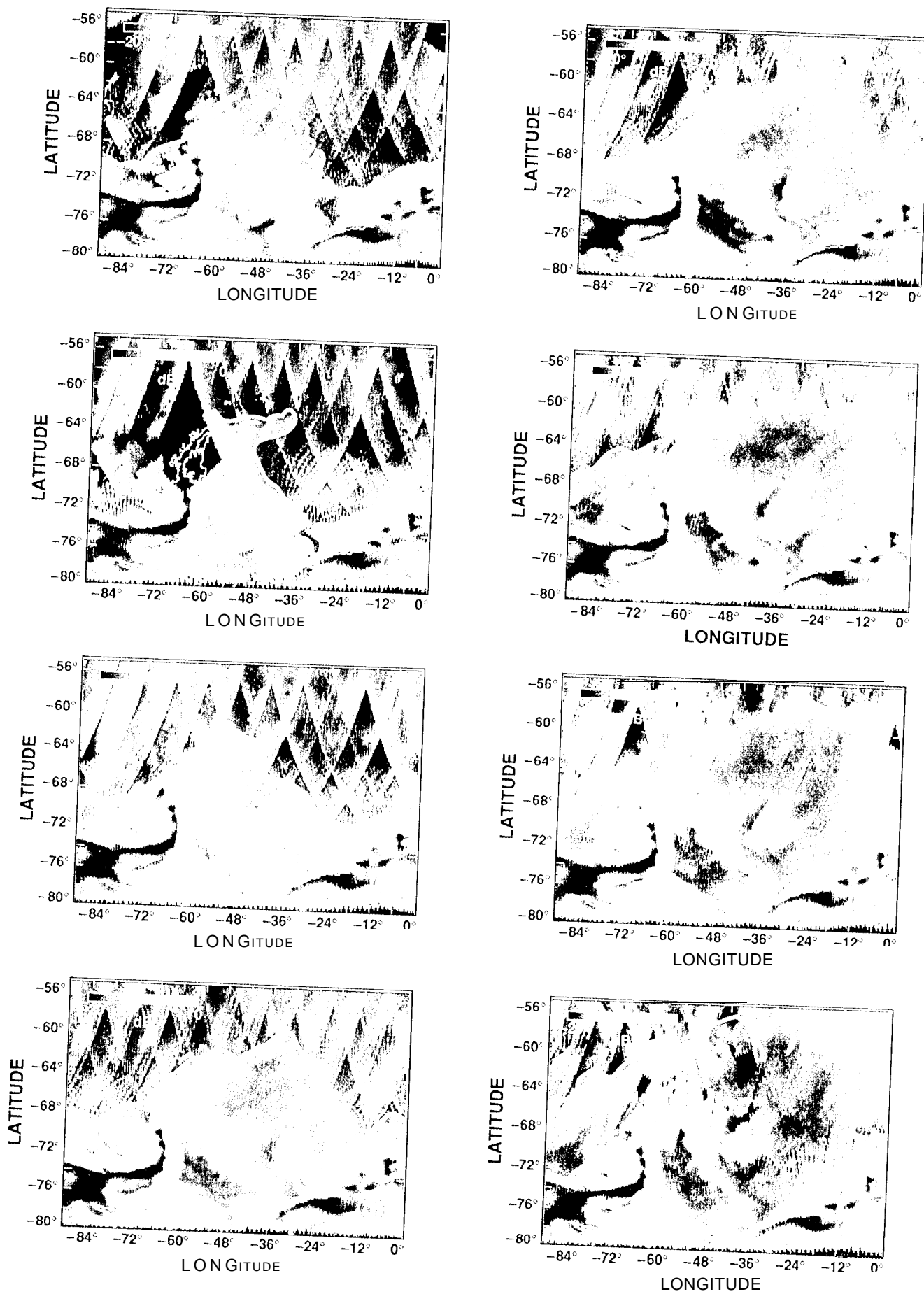


FIGURE 2

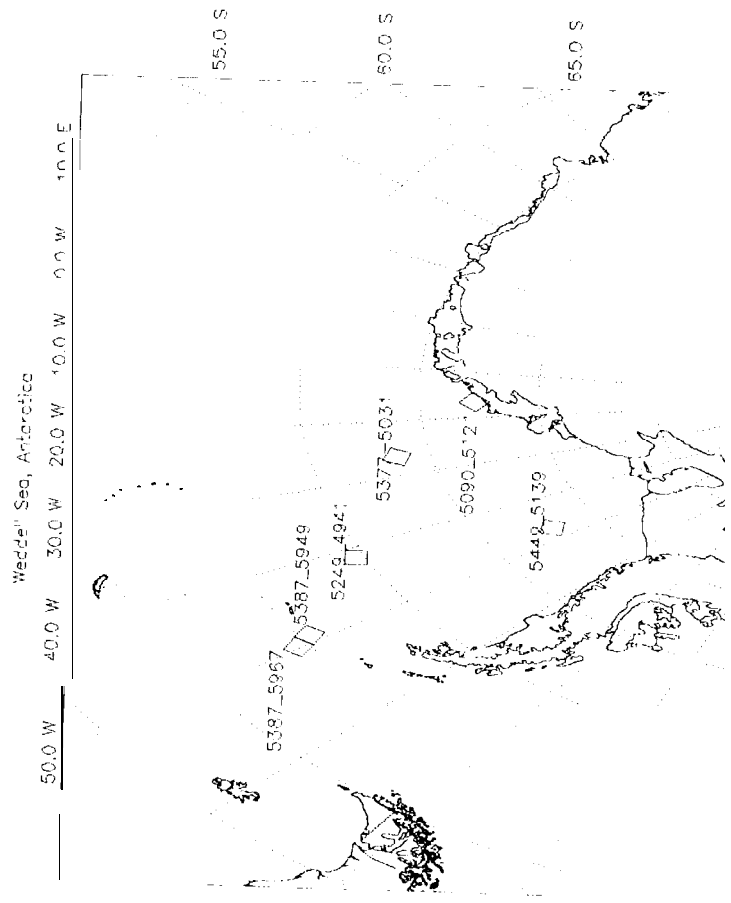


Figure 3.



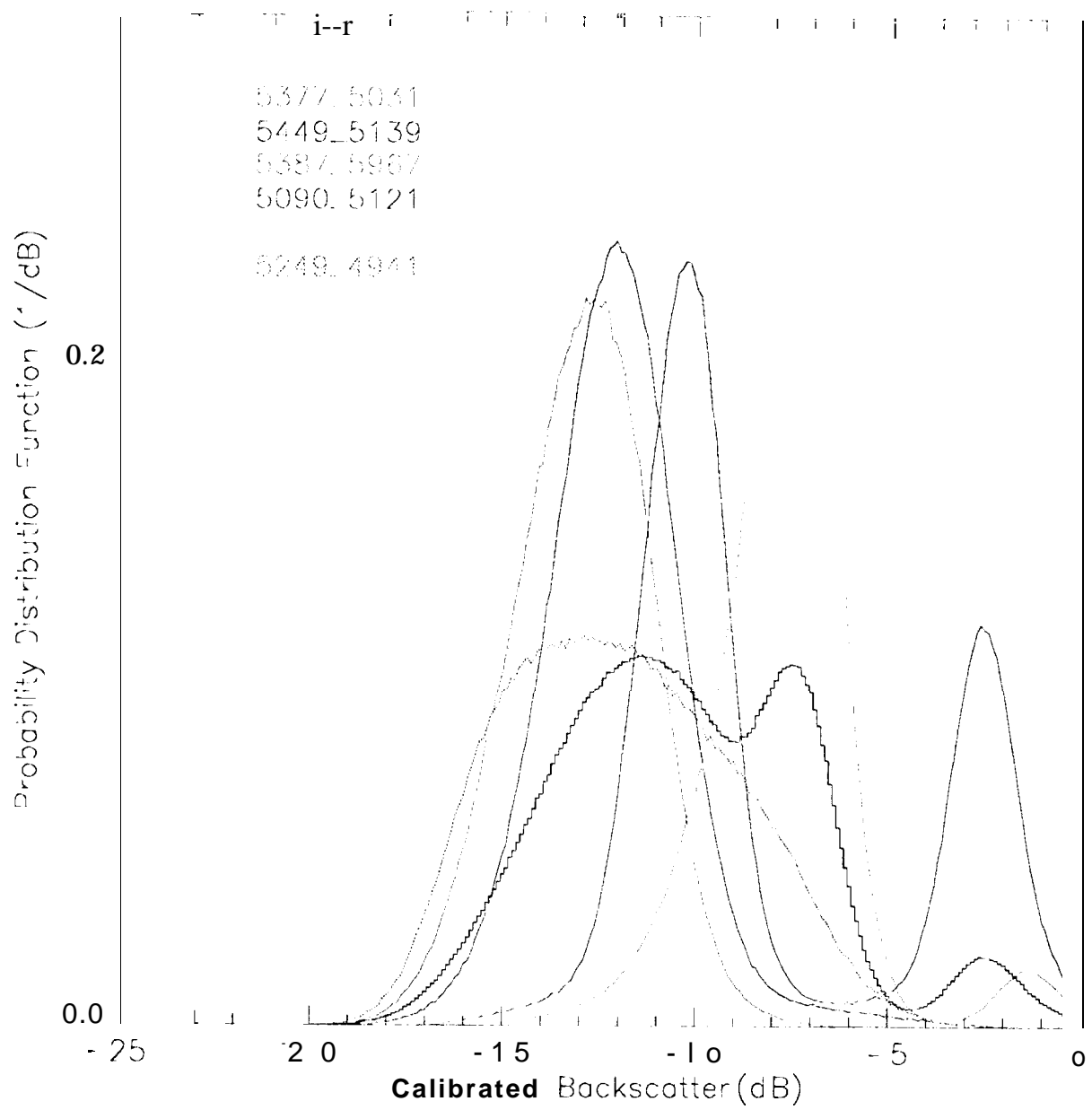


FIGURE 4,

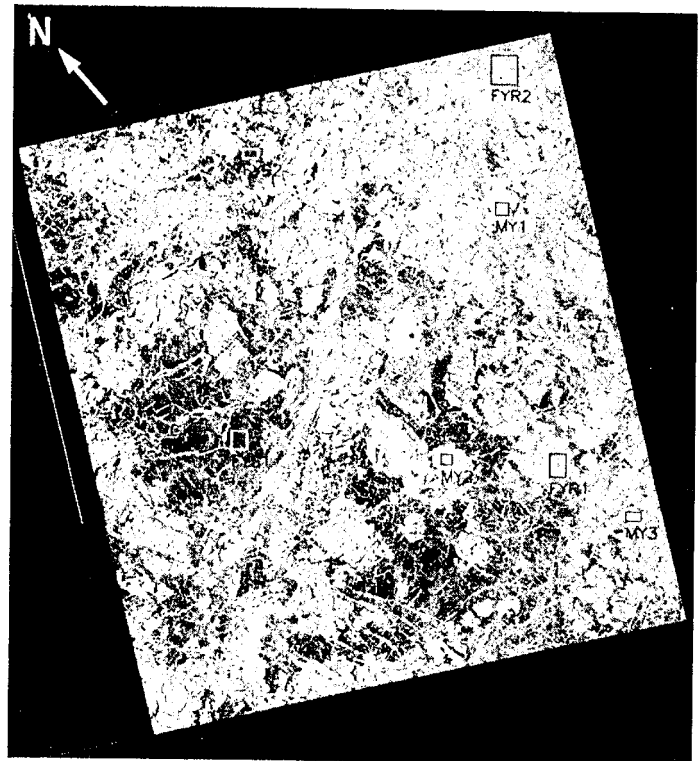
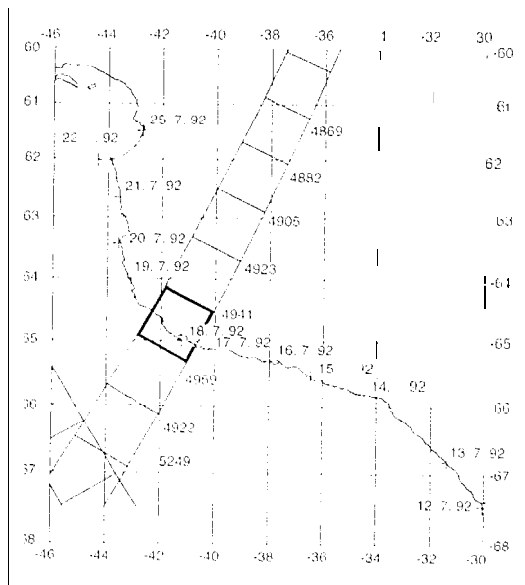


FIGURE 5

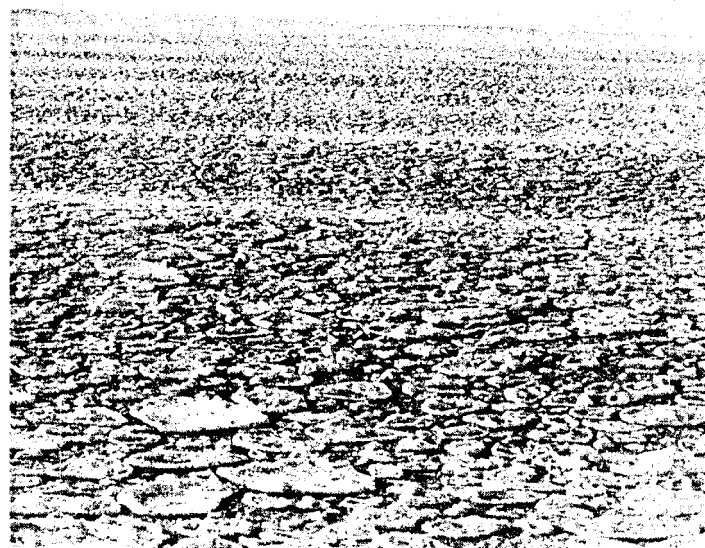
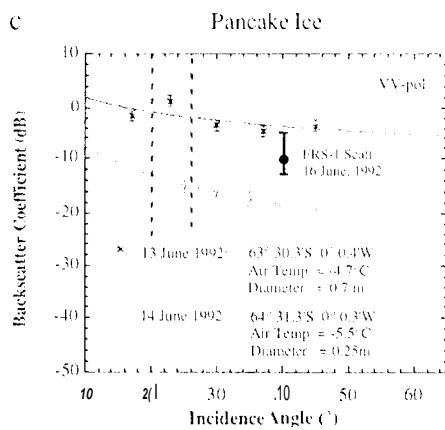
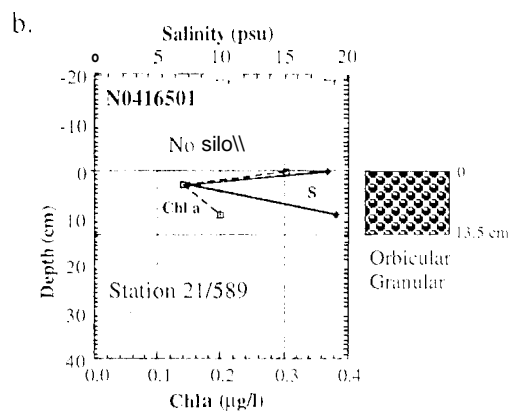


FIGURE 6.

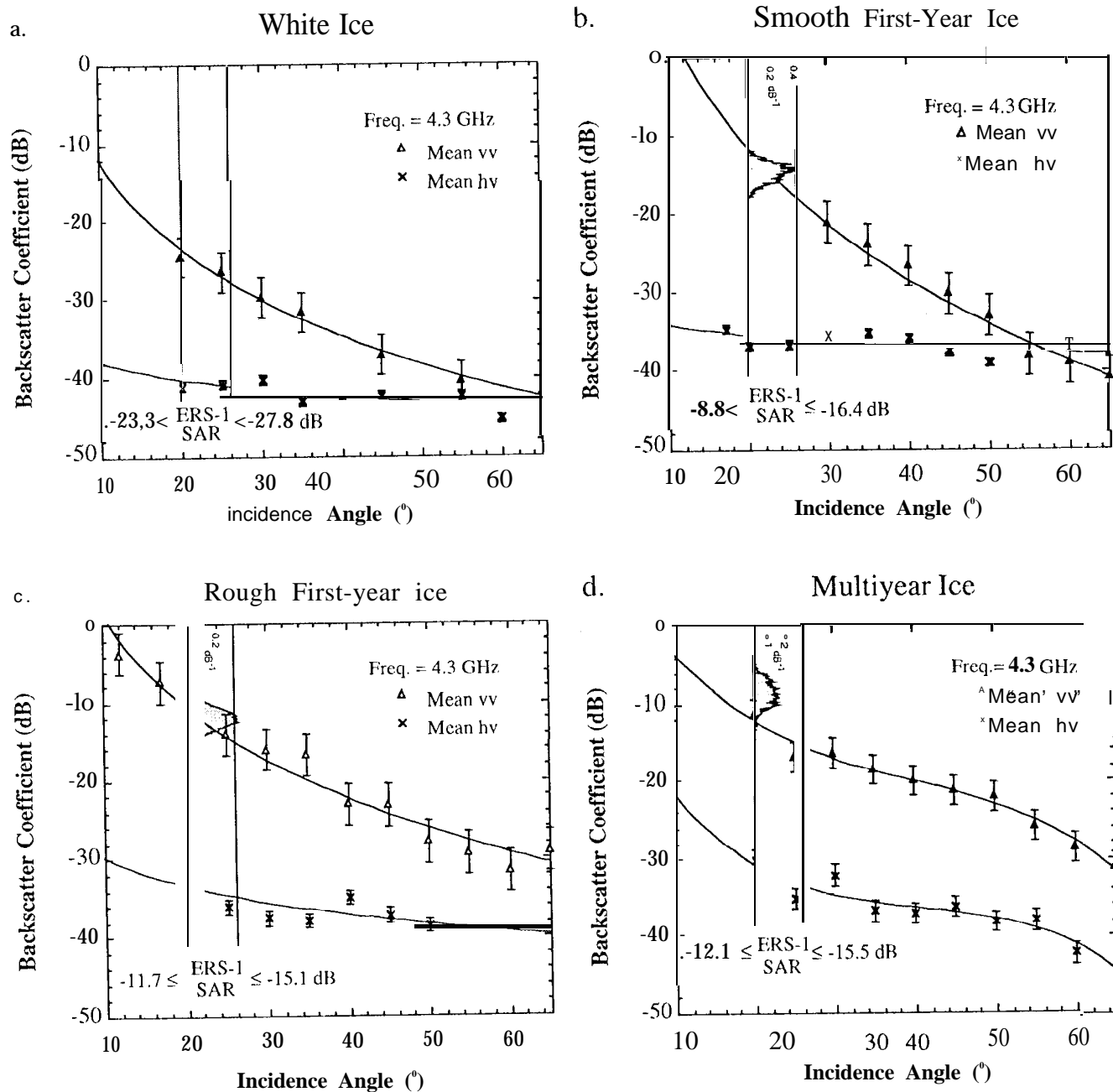


FIGURE 7

# Summary of C-band Weddell Sea Ice Signatures

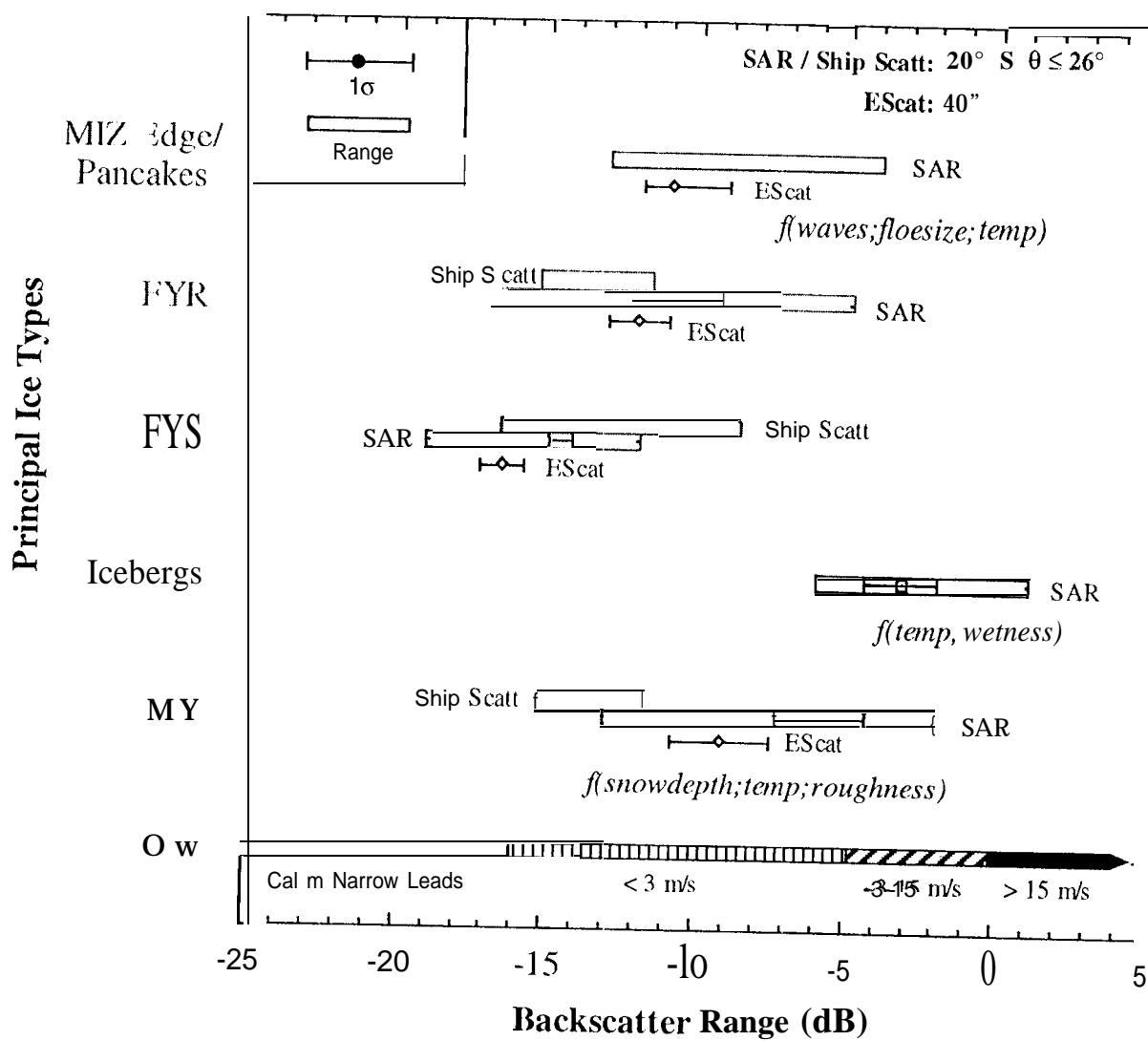


FIGURE 8.

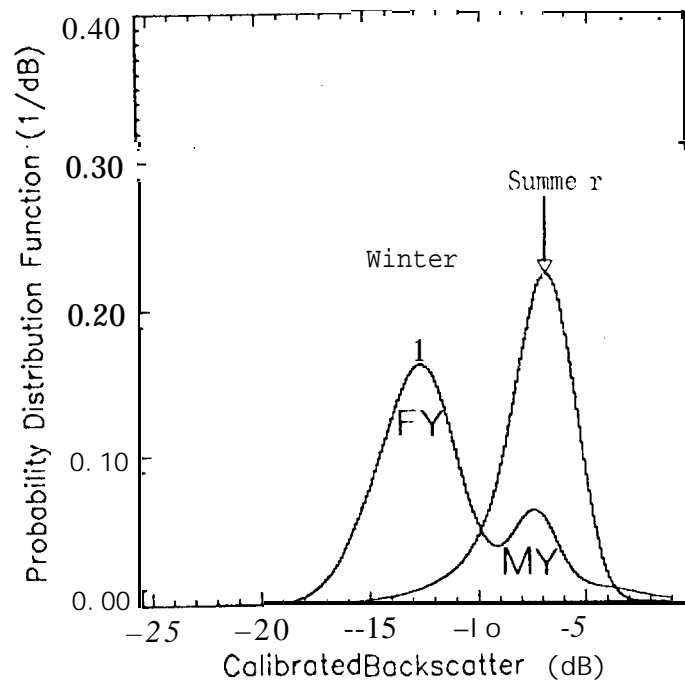


FIGURE 9

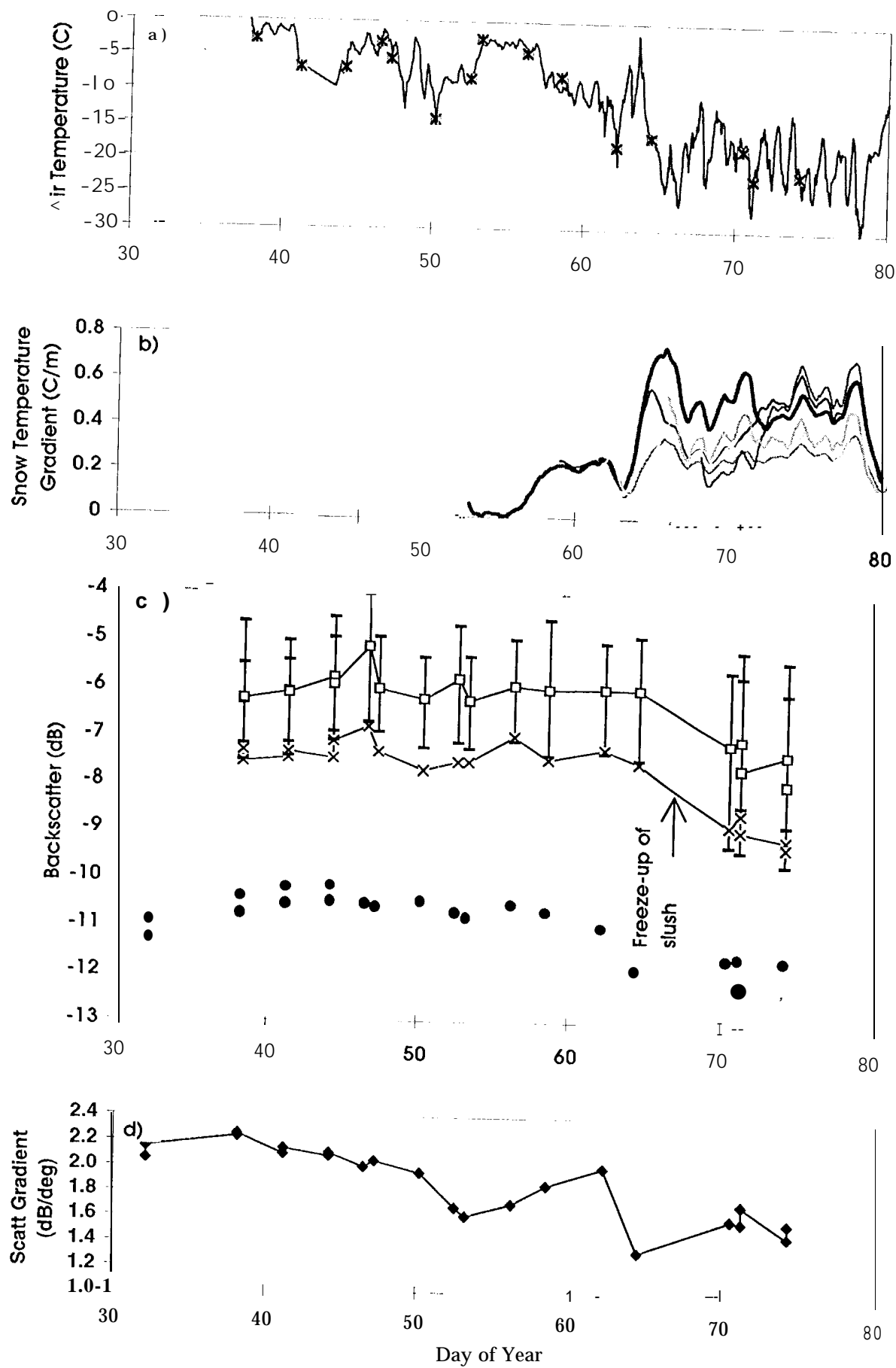


FIGURE 10.

U (cm/s) = -10.4253 +/- 2.47079

V (cm/s) = -5.95165 +/- 2.74263

Start Image: 30585103.dat

Vector File: 30585103.dat

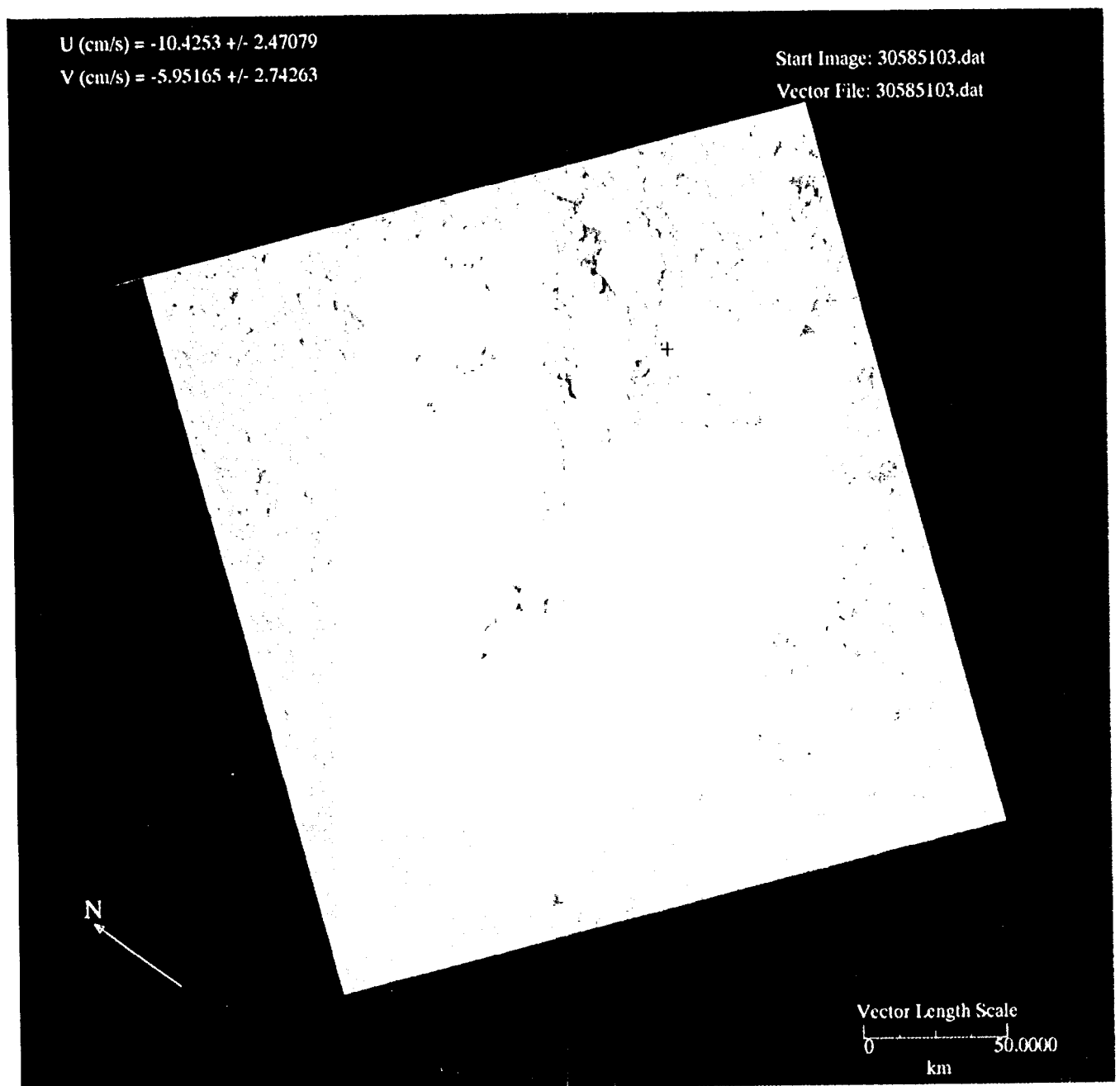


FIGURE 11



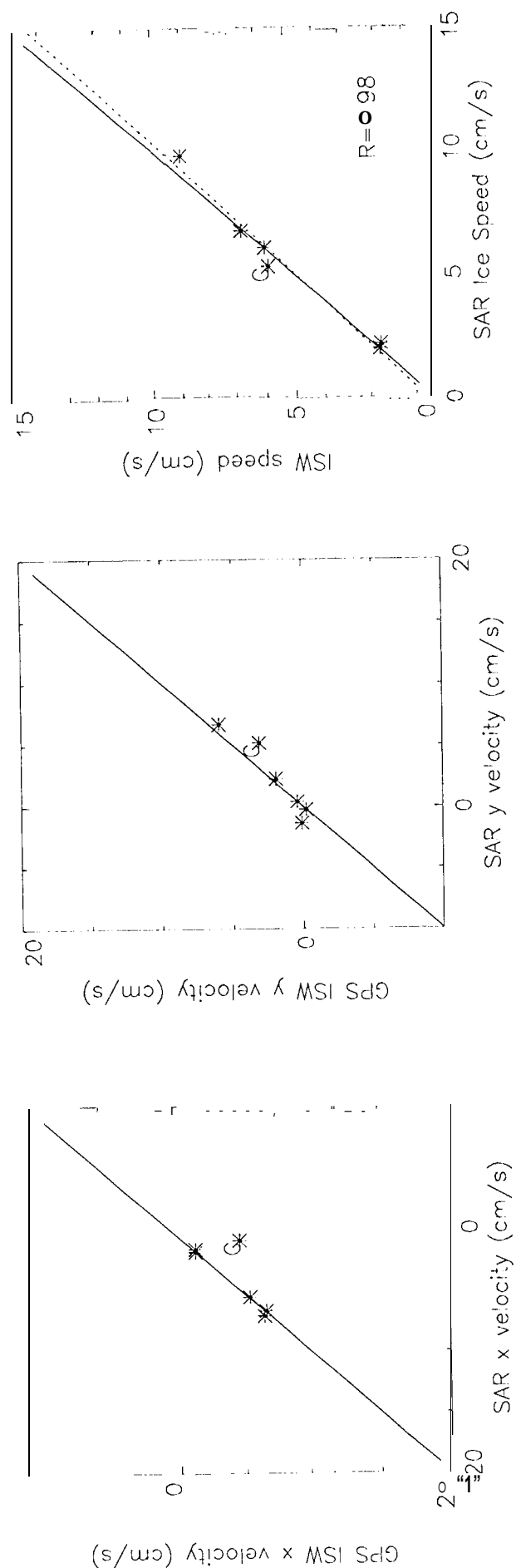


FIGURE 12.

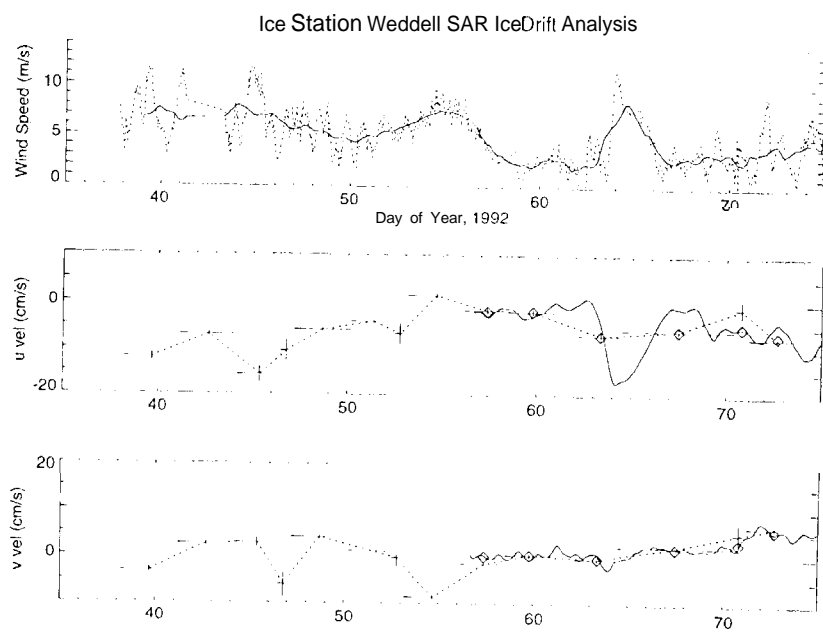


FIGURE 13

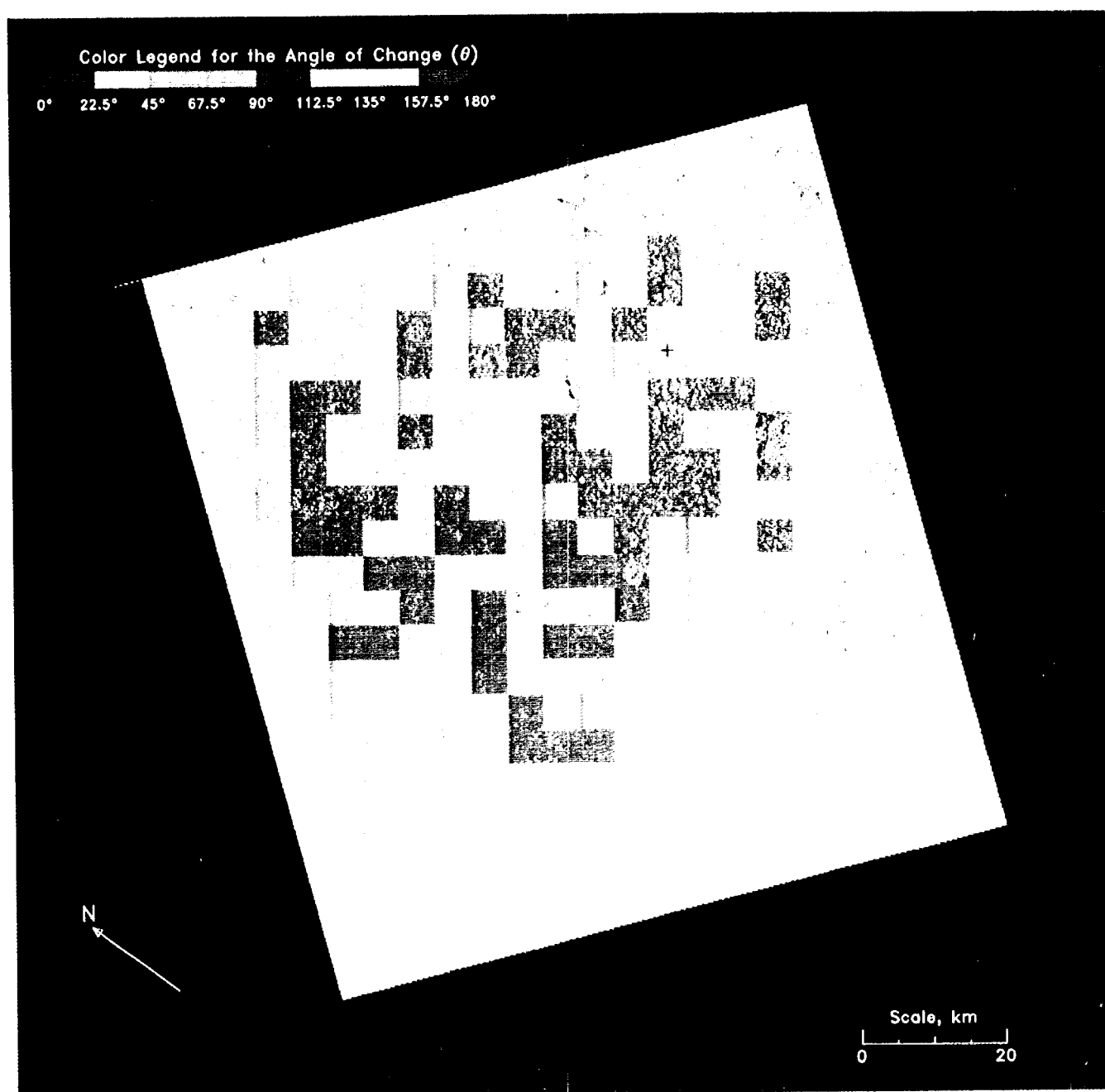


FIGURE 14.

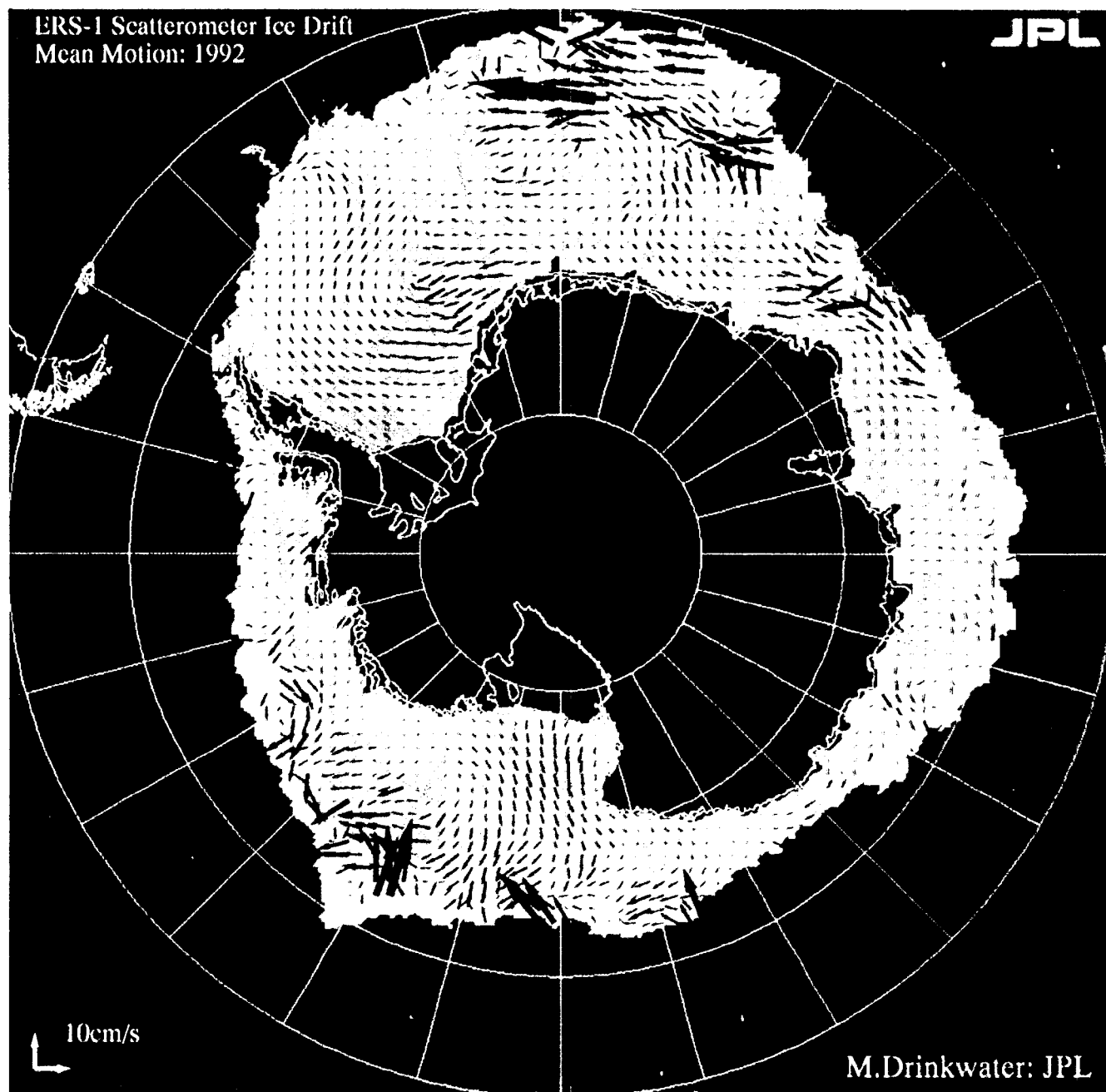


FIGURE 15.